Predicting early-age stress evolution in restrained concrete by thermo-chemo-mechanical model and active ensemble learning

Liang, Minfei; Chang, Ze; He, Shan; Chen, Yu; Gan, Yidong; Schlangen, Erik; Šavija, Branko

DOI
10.1111/mice.12915

Publication date
2022

Document Version
Final published version

Published in
Computer-Aided Civil and Infrastructure Engineering

Citation (APA)
Liang, M., Chang, Z., He, S., Chen, Y., Gan, Y., Schlangen, E., & Šavija, B. (2022). Predicting early-age stress evolution in restrained concrete by thermo-chemo-mechanical model and active ensemble learning. *Computer-Aided Civil and Infrastructure Engineering*, *37*(14), 1809-1833. https://doi.org/10.1111/mice.12915

DOI: 10.1111/mice.12915

RESEARCH ARTICLE

COMPUTER-AIDED CIVIL AND INFRASTRUCTURE ENGINEERING WILEY

Predicting early-age stress evolution in restrained concrete by thermo-chemo-mechanical model and active ensemble learning

Minfei Liang | **Ze Chang** | **Shan He** | **Yu Chen** | **Yidong Gan** | **Erik Schlangen** | **Branko Šavija**

Microlab, Faculty of Civil Engineering and Geosciences, Delft University of Technology, Delft, The Netherlands

Correspondence
Branko Šavija, Microlab, Faculty of Civil Engineering and Geosciences, Delft University of Technology, Delft 2628CN, The Netherlands.
Email: B.Savija@tudelft.nl

Funding information
China Scholarship Council, Grant/Award Numbers: 202007000027, 201806060129

Abstract

Early-age stress (EAS) is an important index for evaluating the early-age cracking risk of concrete. This paper encompasses a thermo-chemo-mechanical (TCM) model and active ensemble learning (AEL) for predicting the EAS evolution. The TCM model provides the data for the AEL model. First, based on Fourier's law, Arrhenius' equation, and rate-type creep law, a TCM model is built to simulate the heat transfer, cement hydration, and viscoelasticity, which together determine the EAS evolution. Then, a material model composed of an eXtreme Gradient Boosting model and adjusted Model Code 2010 is built to allow for parametric study and database construction. Finally, an AEL framework is built, which incorporates principal component analysis (PCA), Gaussian process, and light gradient boosting machine (LGBM). This study resulted in the following findings: (1) The dimensionality of the 672-by-1 EAS vector can be effectively reduced by PCA, and the first principal component (PC) is a global index representing the magnitude of the EAS; (2) the mechanical field of the TCM model is validated by testing data. Correlation analysis on the first PC quantifies the influence of various input parameters of the TCM model, which is in accordance with common understandings of the EAS evolution process. (3) The AEL and one-shot ensemble learning (OSEL) both achieve high prediction performance in the testing set, whose R^2 reaches 0.961 and 0.948, respectively. Thanks to the uncertainty-based query procedure, comparing with OSEL, AEL shows advantages in prediction performance over the whole training history. (4) AEL can significantly reduce the number of samples required for training, which can be a major improvement in efficiency considering the computational cost of the TCM model.

1 | INTRODUCTION

Early-age cracking (EAC) is one of the trickiest engineering problems in the construction of concrete structures. As a combined result of cement hydration reaction, external restraint, and environmental conditions, EAC happens if the early-age stress (EAS) exceeds the tensile strength of concrete. Moreover, even if EAC does not happen, neglecting EAS may cause an underestimation of the internal stress and thus the potential for cracking under service loading. Therefore, to properly evaluate the durability and load-bearing capacity of concrete structures, predicting the evolution of EAS is a significant task in the structural design.

1.1 | Experimental methods

Experimental methods are often the first resort to quantify the EAS or EAC risk under certain circumstances (i.e., mixes, environmental conditions, etc.). Various restraint tests (e.g., rigid cracking frame test—Spingenschmid, 1998; ring test—Briffaut et al., 2016; Gao et al., 2013; internal restraint test—Semianiuk et al., 2017; and Temperature-Stress-Testing-Machine [TSTM] test—Klausen et al., 2019; Shen et al., 2016) were broadly implemented to investigate the influence of different temperature profiles, cementitious materials, creep/relaxation, and different types of shrinkage on the EAS evolution. Among the testing methods mentioned above, the TSTM test stands out with the advantages of temperature control, flexible loading schemes, and tunable restraint degrees (Xin et al., 2020). The TSTM tests are typically conducted on a dog-bone specimen under fully restrained conditions and regulated temperature history. However, despite being a straightforward and accurate testing method, it is not feasible to perform the TSTM test on a wide range of testing parameters due to the following : (1) standard TSTM test requires a complex assembly of precision instruments, including a cryostat, a mold with a water circulation network, linear variable differential transformers (LVDTs) configuration, a loading motor, and so forth. (2) TSTM test is time-consuming because each test typically lasts for 7–28 days. Clearly, conducting a TSTM test for a number of combinations of parameters (e.g., different mixes and environmental parameters) would be laborious, inefficient, and resource intensive. As a result, to quantify the EAS evolution over a wide range of parameters, computer-aided modeling techniques could be an alternative approach to overcome these practical difficulties, allowing, for example, a wide range of parametric studies.

1.2 | Multifield-coupled modeling techniques

EAS evolution is a result of multiple physical and chemical processes occurring during the early age of concrete structures, including the hydration reaction of cement, heat transfer, autogenous shrinkage, drying shrinkage, and creep/relaxation (Azenha et al., 2021; Šmilauer et al., 2019). Hence, to account for the interplay of different mechanisms, multifield-coupled modeling techniques are required. Cervera et al. (1999a, 1999b) proposed a thermo-chemo-mechanical (TCM) model for modeling the early-age concrete behavior. Within a thermodynamic framework, the evolution of concrete properties (i.e., strength, elastic modulus) and behaviors (heat transfer, shrinkage, creep) were simulated, and the EAS evolution was quantified by a viscoelastic damage model. Lackner and Mang (2004) adopted Rankine fracture criterion to build a chemo-plastic material model for EAC analysis, based on the data profiles of temperature and hydration degree of a dam. Gawin et al. (2006a, 2006b) developed a hygro-TCM model to simulate the early-age and long-term concrete behaviors. Based on a solidification-type model, they expressed concrete properties as a function of hydration degree. Then, based on the modified microprestress–solidification theory and effective stress principle, the evolution of creep and shrinkage can be derived, which can finally be used to quantify the EAS evolution using a viscoelastic model. Di Luzio and Cusatis (2009a, 2009b) developed a theoretical hygro-thermo-chemical modeling framework for hydrating concrete and gave a complete guide on numerical implementation, calibration, and validation. By using Fick's law for the moisture transport field, Fourier's law for the heat transfer field, and assuming that the cement hydration reaction follows an Arrhenius-type equation, their model successfully simulated the early-age behavior of concrete such as self-heating and self-desiccation in various scenarios. To summarize, the multifield models in the literature provide a rigorous theoretical framework for simulating the hydration-induced developing properties and deformation of concrete, which are important inputs for modeling the EAS evolution. These models provide a solid basis for further development of multifield models of early-age concrete.

The research in multifield modeling of early-age concrete is still ongoing. Zhao et al. (2020, 2021) coupled the moisture transport field and the heat transfer field and performed an in-depth experimental investigation on the early-age development of temperature and the internal relative humidity. Their multifield-coupled model was shown to achieve high accuracy, compared with the testing results of high-performance concrete. Chiniforush et al. (2022)

built a coupled thermo-mechanical model to investigate the EAS evolution due to thermal shrinkage and delayed ettringite formation. Rather than using only a convective boundary, they considered the effect of radiation in the heat transfer model and adopted mix- and age-dependent heat transfer parameters, which allowed them to obtain good prediction performance in several case studies. However, they also acknowledged that the lack of consideration of creep, which should be considered in all EAS/EAC analyses (Azenha et al., 2021), compromises the applicability of their model. In comparison, Di Luzio and Cusatis (2013) proposed the solidification–microprestress–microplane model to better account for the influence of creep, shrinkage, and thermal deformation on the EAS evolution and EAC risk. To summarize, these multifield models have coupled multiple physical and chemical constitutive equations to describe different material behaviors and have achieved promising performance, compared with experiments. However, although these sophisticated models are effective and accurate, their major disadvantage is a huge demand for computational resources.

1.3 | Significance of this study

An effective way to cope with the dilemma of multifield models mentioned above is through data-driven approaches (or so-called surrogate models, machine learning models, metamodels, etc.), such as the response surface method (Rajashekhar & Ellingwood, 1993), artificial neural network (Lai & Serra, 1997), Gaussian process (GP) regression (F. Kang & Li, 2020), decision tree (Karbassi et al., 2014), random forest (Zhang et al., 2019), and so forth. Unlike coupled multifield models, these data-driven approaches adopt advanced training/fitting algorithms to set up a statistical model with fixed weights, which then directly maps the input parameters of the multifield model or physical experiment to its output objective. In the field of concrete materials and structures, many researchers have successfully implemented such models to predict, for example, autogenous shrinkage (Hilloulin & Tran, 2022), drying shrinkage (Bal & Buyle-Bodin, 2013), creep (Liang, Chang, et al., 2022; Liang, Gan, et al., 2022), crack propagation (Bayar & Bilir, 2019), compressive strength (Marani et al., 2020), elastic modulus (Han et al., 2020), breakout capacity (Olalusi & Spyridis, 2020), shear capacity (Solhmirzaei et al., 2020), slump flow (Gomaa et al., 2021), flexural strength (M. C. Kang et al., 2021), interfacial bond strength (Su et al., 2021), and so forth. However, although data-driven models require significantly less computational resources than multifield models, their major challenge is the generalization capability (i.e., how to ensure that the data-driven models make good predictions not only on training data but also on unseen data?). Furthermore, due to the complexity of the multifield-coupled model, only a limited dataset size can be available for the training process, which cannot cover a wide range of variables (e.g., temperature, age) related closely to the EAS evolution, and this can compromise the training effectiveness. To cope with the challenges mentioned above, the following objectives are worth considering: (1) Underfitting/overfitting should be prevented; and (2) an efficient sampling strategy should be developed.

In view of the first objective, the types of surrogate models and corresponding hyperparameters should be selected to achieve a variance-bias tradeoff. In this regard, ensemble learning models outperform many other standalone models by combing simple models into a strong one (Sagi & Rokach, 2018). Based on classical ensemble strategies like bagging (Breiman, 1996, 2001) or gradient boosting (Chen & Guestrin, 2016; Ke et al., 2017), ensemble learning models have not only won many championships in various machine learning competitions but have also achieved excellent performance in predicting concrete properties and behaviors (Asteris et al., 2021; Cai et al., 2020; Liang, Chang, et al., 2022).

In view of the second objective, an active learning process should be developed, by which the surrogate model is adaptively trained based on a selective set of data samples. The selection criterion of data sample in each active learning step is based on the uncertainty of the surrogate model measured by the variance distribution over the whole sample pool. To measure the uncertainty of the surrogate model, the GP method stands out with its probabilistic nature, in which not only a mean is given as the prediction, but also a variance is given as the uncertainty of the corresponding prediction (Rasmussen & Williams, 2006). Taking advantage of this, very efficient GP-based global optimization techniques (Jeong et al., 2005; Jones et al., 1998) were developed for the optimization of complex engineering problems, which have high-dimensional parameters and depend on computationally expansive models. In the field of civil engineering, relevant studies on GP-based active learning are still rare. In recent years, studies (Tomar & Burton, 2021; Yuan et al., 2022) of GP-based active learning in reliability analysis have started to emerge, in which learning functions like expected improvement function (Jones et al., 1998), expected feasibility function (EFF; Bichon et al., 2008) and U function (Echard et al., 2011) have been implemented to quantify the potential contribution of a certain sample point to the improvement of the prediction performance of the surrogate model. Such potential contribution is mainly quantified by the distance of the sample point to the limit state boundary and the uncertainty. In other words, the sample points that are more likely to induce structural

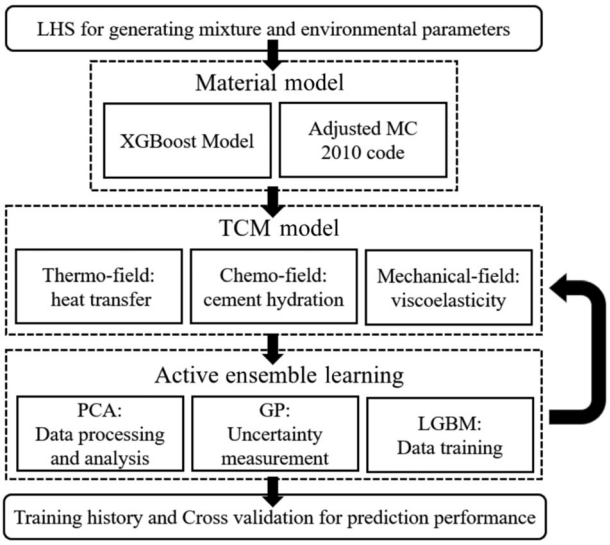

FIGURE 1 Work flow of this paper

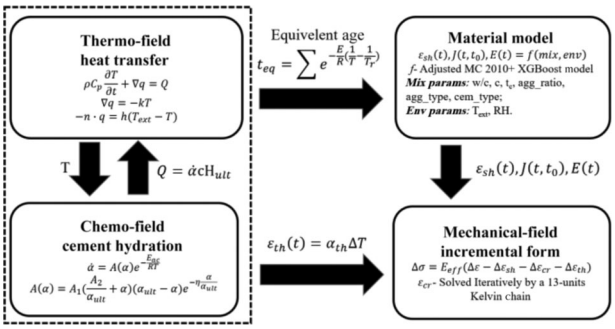

FIGURE 2 Formulation of the thermo-chemo-mechanical (TCM) model

failure and the sample points on which the surrogate model has high uncertainty will be selected so as to achieve the exploitation–exploration tradeoff. Studies (Tomar & Burton, 2021; Yuan et al., 2022) have exemplified that GP-based active learning can achieve high accuracy in structural reliability analysis with only dozens of data samples in the training set.

This paper develops an active ensemble learning (AEL) model, which is trained using the data generated by a TCM model for efficiently predicting the EAS evolution. The workflow of this paper is shown in Figure 1. The sampling space is first generated by the Latin hypercube sampling (LHS) method and processed by a material model, which is built by an eXtreme Gradient Boosting (XGBoost) machine learning model and Model Code 2010 (MC 2010; fib, 2013). Based on Fourier's law, an Arrhenius' equation, the maturity concept, and the rate-type creep law (Bažant & Jirásek, 2018), the TCM model is built to simulate the hydration effects, thermal deformation, creep/relaxation of concrete, and run incremental viscoelastic analyses of EAS evolution. In the AEL process, principal component analysis (PCA) will be conducted first to reduce the dimensionality of the EAS vector and perform correlation analysis. The AEL process uses a GP model to measure the uncertainty for active sampling and train a light gradient boosting machine (LGBM) on the selective sample. In each learning step, the most uncertain sample (measured by the variance distribution) is selected by the GP model and imported to the TCM model as input. The EAS output by the TCM model is then used to update the GP model and the LGBM model. By cross-validation, the generalization capabilities of AEL are quantified and compared with one-shot ensemble learning (OSEL).

2 | TCM MODEL

The formulation of the multifield TCM model is shown in Figure 2. In previous studies (di Luzio & Cusatis, 2009a, 2009b; Zhao et al., 2020, 2021) on multifield modeling of early-age concrete, the applicability of Fourier's law for heat transfer and Arrhenius's equation for hydration reaction were validated. These two constitutive equations are also adopted in this work to simulate the thermo- and chemo-fields of the TCM model. The thermo- and chemo-fields are fully coupled by the temperature and hydration degree: The temperature distribution output by the thermo-field is in the exponential term of the hydration degree kinetics in the chemo-field, while the hydration degree output by the chemo-field is in the heat source term of the thermo-field. In the TCM model, the temperature distribution/evolution influences the hydration kinetics and results in different developing speeds of the concrete properties and behaviors. This impact is quantified by the equivalent age of the maturity concept as shown in the upper arrow connecting the TC-field and material model in Figure 2. On the other hand, the temperature distribution/evolution induces thermal deformation, which is restrained by the boundary and is one of the major deformations that cause EAS. This impact is quantified linearly by a coefficient of expansion as shown in the lower arrow connecting the TC-field and material model in Figure 2.

Note that the hygro-field, which is important for the behavior of shrinkage and creep, is not considered in this paper due to the following reasons: (1) general formulas of material parameters involved in hygro-field are scarce; (2) the mechanisms of autogenous shrinkage, drying shrinkage, and creep induced by moisture transport are still under debate; (3) the heterogeneity of concrete plays an important role in the hygro-field, and the mechanisms for building a micro- or meso-scale model for a wide range of practical cases are not clear. In view of these complexities, this paper assumes the concrete as a homogeneous and isotropic material and refers to the MC 2010 to retrieve the

input of shrinkage and creep from empirical formulas. The material model is constructed by an XGBoost model and an adjusted MC 2010. The XGBoost is used to predict the compressive strength based on given mixture parameters. Subsequently, the compressive strength is used as one of the input parameters for the MC 2010. Thereby, the material model can output the evolution of shrinkage, creep compliance, and elastic modulus, which provide input for the TCM model.

The mechanical field is formulated by a 13-unit Kelvin chain rheological model and solved incrementally by the exponential algorithm (Bažant & Chern, 1985). The mechanical field adopted in this work has been discussed and validated based on the TSTM tests performed by the authors (see Liang, Li, et al., 2022). Taking the output of the material model and the TC field, the mechanical field can output the EAS evolution (i.e., a 672-by-1 vector), which is prepared for the further AEL process.

2.1 | Chemo-field

When cement is in contact with water, the unhydrated particles including calcium silicates (C_3S, C_2S), calcium aluminates (C_3A), and calcium aluminoferrites (C_4AF), react with free-water and produce calcium silicate hydrates (C-S-H), calcium hydroxide (CH), ettringite (Aft), and monosulfate (Afm; Taylor, 1997). Although the microstructure development of cement in the process of hydration reaction can be simulated numerically (Breugel, 1991; Thomas et al., 2011; Ye et al., 2003), a general and reliable multiscale strategy for upscaling the micro-scale microstructure evolution to macro-scale concrete behavior is still not available. The exact stoichiometry of the hydration reactions and the influence of the environment still cannot be precisely quantified. In this paper, the hydration reaction is simulated as an overall hydration process, similar to many other multifield models (Cervera et al., 1999a, 1999b; di Luzio & Cusatis, 2009a, 2009b; Gawin et al., 2006a, 2006b). Assuming that the hydration kinetics can be described by postulating the existence of a Gibb's free energy dependent on temperature and hydration extent, the hydration reaction can be described by the following Arrhenius-type equation (Cervera et al., 1999a; di Luzio & Cusatis, 2009a; Ulm & Coussy, 1995):

$$\dot{\alpha} = A(\alpha) e^{-\frac{E_{ac}}{RT}} \tag{1a}$$

$$A(\alpha) = A_1 \left(\frac{A_2}{\alpha_{ult}} + \alpha \right) (\alpha_{ult} - \alpha) e^{-\eta \frac{\alpha}{\alpha_{ult}}} \tag{1b}$$

where α is the hydration degree; the $(\cdot)$ in Equation (1a) represents the first-order derivative with respect to time; E_{ac} is the apparent activation energy; R is the universal gas constant; T is the temperature; η, A_1, and A_2 are fitting parameters corresponding to a certain type of cement, which can be calibrated according to adiabatic test results (di Luzio & Cusatis, 2009a); α_{ult} is the ultimate hydration degree dependent on the water–cement ratio, which can be expressed as (Pantazopoulou & Mills, 1995):

$$\alpha_{ult} = \frac{1.031 w/c}{0.194 + w/c} \tag{2}$$

In this study, three sets of fitting parameters η, A_1, and A are used to represent three cement types (i.e., SL, N, R), as classified by the MC 2010 (fib, 2013). The value for apparent activation energy E_{ac} is dependent on the cement type and temperature. The activation energy decreases with temperature when the temperature is lower than 20°C but remains constant when the temperature is equal to or higher than 20°C (Breugel, 1991). Based on tests, the following bilinear relationship for apparent activation energy has been proposed (Hansen & Pedersen, 1977):

$$E_{ac} = \begin{cases} E_{ac,0}, \text{ if } T \geq 20°\text{C} \\ E_{ac,0} + 1470\,(20 - T), \text{ if } T < 20°\text{C} \end{cases} \tag{3}$$

where $E_{ac,0}$ is the apparent activation energy of a certain cement type at 20°C. The specific parameters can be found in Section 3.3. At every time step, the output of the hydration degree α of the chemo-field is used to compute the hydration heat of cement, which is the heat source term of the thermo-field as will be shown in Section 2.2.

2.2 | Thermo-field

When the temperature is below 100°C, the heat conduction in concrete can be described by Fourier's law (Hansen & Pedersen, 1977):

$$\rho C_p \frac{\partial T}{\partial t} + \nabla q = \dot{Q} \tag{4a}$$

$$\nabla q = -kT \tag{4b}$$

$$-n \cdot q = h(T_{ext} - T) \tag{4c}$$

where ρ is the density of concrete; ∇ is the Nabla operator that calculates the spatial gradient, $\nabla = (\frac{\partial}{\partial x}, \frac{\partial}{\partial y}, \frac{\partial}{\partial z})$;

C_p is the heat capacity; q is the heat flux; k is the thermal conductivity. Note that Equation (3c) is the convective boundary attached to the surface of the concrete specimen, where n is the normal vector of the specimen surface; h is the heat transfer coefficient, and T_{ext} is the environmental temperature. The internal heat source term $Q^{\cdot}$ in Equation (3a) represents the heat release rate of cement hydration, which can be calculated by the hydration degree from the chemo-field, expressed as follows (Cervera et al., 1999a):

$$\dot{Q} = \dot{\alpha}\, cQ_{ult} \tag{5}$$

where c is the cement mass, Q_{ult} is the ultimate heat release of the hydration reaction per unit weight of cement, which is determined by the cement composition and can be measured by calorimetric tests. Typical values of Q_{ult} range from 400 kJ/kg to 550 kJ/kg (Bazant & Kaplan, 1996). In this paper, three sets of values of Q_{ult} will be adopted to represent three types of cement (see Section 3.3). The temperature distribution output by the thermo-field influences the hydration process (see Equation 1a), which ensures the full two-way coupling between the thermo- and the chemo-fields.

In addition, the temperature distribution output by the thermo-field induces thermal deformation, expressed as

$$\varepsilon_{th}\ (t) = \alpha_{th}\, \Delta T \tag{6}$$

where α_{th} is the linear coefficient of thermal expansion (a constant value of 1.0×10^{-5}[1/K] is adopted herein; Bentz, 2008). On the other hand, the temperature distribution output by the thermo-field also determines the equivalent age of concrete, calculated by the maturity concept (Hansen& Pedersen, 1977):

$$t_{eq} = \sum e^{-\frac{E_{ac}}{R}\left(\frac{1}{T}-\frac{1}{T_r}\right)} \tag{7}$$

where t_{eq} is the equivalent age; T_r is the reference temperature, which is 20°C in this paper. The equivalent age t_{eq} calculated in Equation (7) will be used as the index of time to query the concrete properties and behavior from MC 2010. In the adopted material model MC 2010, the use of maturity concept is only explicitly suggested in calculating the loading age of creep. This paper uses the maturity concept also in the calculation of the time duration of both creep (De Schutter, 2004) and shrinkage (Turcry et al., 2002). However, it should be noted that the maturity concept may not be able to fully account for the influence of temperature on creep and shrinkage (Chu et al., 2012) and more fundamental studies are needed to derive a more reliable material model regarding the influence of temperature.

2.3 | Mechanical field

With the temperature output from the thermo- and chemo-field, the thermal deformation of the concrete can be determined. Meanwhile, the evolving properties and behaviors (i.e., shrinkage, creep) can be queried from MC 2010 based on the maturity concept and used as input for the mechanical field to carry out the EAS computations.

The EAS is a direct index for evaluating the EAC risk by analyzing the stress levels or cracking indexes (i.e., the ratio between the stress level and the tensile strength). In this study, the mechanical field focuses on the EAS evolution in the pre-cracking stage; therefore, local cracks and damages in stress singular points are disregarded as recommended by the study (Azenha et al., 2021). Besides, the majority of the creep models assume that no damage occurs, and general formulas allowing for parameterization over a wide range of concrete properties and damage status are scarce. Thereby, the mechanical field of this study takes the viscoelasticity of concrete as the main mechanical constitutive model to compute the EAS evolution. Based on Boltzmann superposition, the EAS evolution initiated from different time of loading (i.e., each timing when restrained shrinkage happens) is quantified and expressed as the following convolution:

$$\sigma\ (t) = \int_0^t R\left(t, t'\right) \mathrm{d}\varepsilon\left(t'\right) \tag{8}$$

where R is the relaxation function; t is the age of concrete; t' is the time of loading; ε is the imposed strain that is applied by the boundary condition. The convolution of Equation (8) requires to store the strain history $\varepsilon(t)$ of every element in the finite element mesh and can easily cause a shortage of memory. Therefore, this paper incorporates the rate-type creep law to avoid this complex integration by incrementally solving a quasi-elastic equation (Bažant & Jirásek, 2018; di Luzio et al., 2020). First, due to the fact that the experimental measurement of relaxation function R is practically untenable (Bažant & Jirásek, 2018), Equation (8) is written in the form of creep integration as

$$\varepsilon\ (t) = \int_0^t J\left(t, t'\right) \mathrm{d}\sigma\left(t'\right) \tag{9}$$

where J is the creep compliance function. Assuming a linear stress variation within each time step, the following incremental form of Equation (9) can be obtained:

$$\Delta\sigma\ = E^*\, \Delta\varepsilon - \sigma^* \tag{10a}$$

$$E^* = \frac{\Delta t}{\int_{t_i}^{t_{i+1}} J\left(t_{i+1}, t'\right) dt'} \tag{10b}$$

$$\sigma^* = E^* \int_0^{t_i} \left[J\left(t_{i+1}, t'\right) - J\left(t_i, t'\right)\right] \dot{\sigma} dt' \tag{10c}$$

where $\Delta\sigma$ and $\Delta\varepsilon$ are the incremental stress and strain between two consecutive time steps t_i and t_{i+1}, respectively. The creep compliance function is expressed as a Dirichlet series, which in the meantime is the governing equation of the Kelvin chain rheological model with N sets of spring and dashpot:

$$J\left(t, t'\right) = \frac{1}{E_0\left(t'\right)} + \sum_{j=1}^{N} \frac{1}{E_j\left(t'\right)} \left(1 - e^{-\frac{t-t'}{\mu_j}}\right) \tag{11}$$

where E_j and μ_j are the elastic moduli and retardation time of jth Kelvin chain units. By substituting the creep compliance $J(t, t')$ in Equation (11) for the $J(t, t')$ in Equation (10) and calculating the integral by mid-point rule, the E^* and σ^* in Equation (10) can be obtained as (Bažant & Jirásek, 2018; di Luzio et al., 2020):

$$E^*\left(t^*\right) = \frac{1}{\frac{1}{E_0(t^*)} + \sum_{j=1}^{N} \frac{1}{E_j(t^*)} \left(1 - \left(1 - e^{-\frac{\Delta t}{\mu_j}}\right) \frac{\mu_j}{\Delta t}\right)} \tag{12a}$$

$$\sigma^*(t_i) = E^*\left(t^*\right) \sum_{j=1}^{N} \left(1 - e^{-\frac{\Delta t}{\mu_j}}\right) \varepsilon_j^*(t_i) \tag{12b}$$

$$\varepsilon_j^*(t_i) = \int_0^{t_i} \frac{1}{E_j\left(t'\right)} e^{-\frac{t_i - t'}{\mu_j}} \dot{\sigma} dt' \tag{12c}$$

$$\varepsilon_j^*\left(t_{i+1}\right) = e^{-\frac{\Delta t}{\mu_j}} \varepsilon_j^*(t_i) + \frac{1}{E^*(t_i)} \left(1 - e^{-\frac{\Delta t}{\mu_j}}\right) \frac{\mu_j}{\Delta t} \Delta\sigma \tag{12d}$$

where t^* is the average of two consecutive time steps t_i and t_{i+1}. Equations (10a) and (12) form the incremental quasi-elastic constitutive equation of the mechanical field.

2.4 | Multifield model configuration

2.4.1 | Continuous Kelvin chain

The mechanical field is characterized by the rheological model Kelvin chain with multiple sets of sequentially connected springs and dashpots as specified by Equation (11). In this paper, a 13-unit spring-dashpot Kelvin chain is used. The Kelvin chain parameters (i.e., elastic modulus and viscosity in each unit) calculated here have an error range of 2% in the fitting process of the creep compliance and covers a wide range of time steps (Liang, Li, et al., 2022). Specific parameters of this Kelvin chain should be derived from the creep compliance surface $J(t, t')$ obtained from the material model, which can be written as the following double-power law:

$$J\left(t, t'\right) = \frac{1}{E\left(t'\right)} + C_0\, C_1\left(t'\right) C_2\left(\xi\right) \tag{13}$$

where C_0 is a constant coefficient; C_1 is a power function to describe the aging of creep compliance; C_2 is a power function representing the non-aging term, which mainly depends on the time of loading ξ ($\xi = t\text{-}t'$). Specific settings for these three parameters can be obtained from MC 2010 (fib, 2013). To fit the result of Equation (13) into Equation (11), Bažant's fitting procedure is adopted, which guarantees a unique and stable solution for a continuous Kelvin chain (Bazant et al., 1995; Carol & Bažant, 1993). First, the retardation time μ_j is specified to prevent the system of equations from becoming ill-conditioned:

$$\mu_j = 10^{(-6+j)}, \qquad j = 1 : 13 \tag{14}$$

Then, the continuous form of the non-aging term C_2 can be written as

$$C_2\left(\xi\right) = \int_0^{\infty} \frac{1}{E_j} \left(1 - e^{-\frac{\xi}{\mu_j}}\right) \mathrm{d}\left(\ln \mu_j\right) \tag{15}$$

Performing Laplace transform and applying Widder's formula, the solutions of E_j can be written as

$$\frac{1}{E_j} = -\ln 10 * \lim_{k \to \infty} \frac{(-k\mu)^k}{(k-1)!} C_2^{(k)}(k\mu) \tag{16}$$

In this paper, the spectrum of third order ($k = 3$) is used, which is sufficient for obtaining a Kelvin chain to mimic the code with a small error within 2% (Liang, Li, et al., 2022).

2.4.2 | Finite Elelment Model (FEM) configuration

The geometry of the dog-bone specimen in the TSTM test (Liang, Li, et al., 2022; Lokhorst, 2001) is used in the TCM model, which has a 100*150*850 mm^3 prism in the middle, and two clamping heads at the two ends. The dog-bone specimen simplifies structural factors (geometry,

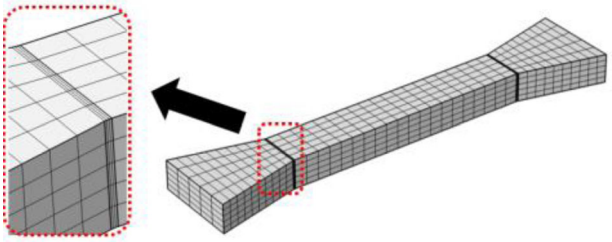

FIGURE 3 Meshing scheme of the Temperature-Stress-Testing-Machine (TSTM) specimen

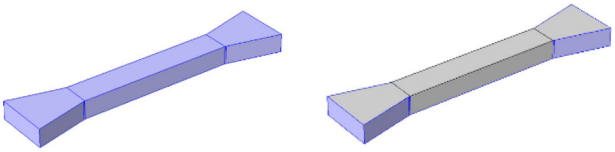

FIGURE 4 Boundary conditions (highlighted area): (a) convective boundary, (b) roller boundary

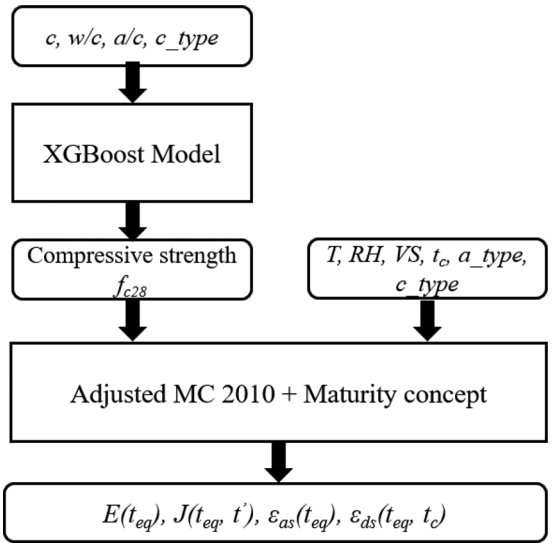

FIGURE 5 Formulation of the material model

boundary conditions), which can significantly vary from case to case and are difficult to parametrize in a single model. Moreover, considering that the EAC is intrinsically caused by the material behavior (e.g., shrinkage and creep), the TSTM test configuration (and therefore and standard the TCM-based AEL model) is used as a general scenario for EAC risk evaluation. Hexahedral elements are used to mesh the whole specimen. Finer mesh is applied at the two ends of the middle prismatic part as shown in Figure 3. A study on the influence of mesh size on the modeling results was performed in the author's previous work (see Liang, Li, et al., 2022), by changing the number of elements from 270 to 6318. It was found that the EAS results remain constant after increasing the number of elements from 1150 to 6318. Therefore, the number of elements in the current meshing scheme is taken as 1150 and the mesh size varies from 25 to 145 mm.

The boundary conditions for the thermo- and mechanical field are shown in Figure 4. A convective boundary is applied to all surfaces of the specimen to determine the heat transfer between the specimen and the environment (see Equation 4c). Roller boundary, which restricts the normal deformation of the surface to 0, is attached to the lateral surface of the two ends of the dog-bone specimen.

To solve the system of ordinary and partial differential equations formed by the thermo-field (Equations 4 and 5), chemo-field (Equation 1) and mechanical field (Equilibrium equation $\nabla\sigma + F_V = 0$, strain–strain equation $\varepsilon = \frac{1}{2}(\nabla u + (\nabla u)^T)$, and viscoelastic constitutive equation (Equations 10 and 12), the backward difference method and the damped Newton method are adopted to obtain convergent numerical solutions. Detailed procedures regarding the numerical solver can be found in (Hoffman et al., 2018; Stute et al., 2013). A fixed time step (i.e., Δt) when conducting the backward difference method is needed due to the mid-point integration approximation in Equation (12). In this paper, a time step of 1 h is used, and the time range of interest is from 0 to 672 h.

3 | MATERIAL MODEL

The formulation of the material model is shown in Figure 5. First, the mixture parameters are imported to an XGBoost model (Chen & Guestrin, 2016) for compressive strength prediction. Then, based on the predicted compressive strength and other parameters such as the ambient temperature and relative humidity, the MC 2010 model provides elastic modulus, creep, and shrinkage, which can be finally imported to the TCM model and used to calculate the EAS development. To consider a practical case of EAC, this study uses the following eight input parameters for the TCM model and AEL model: (1) *c*: cement mass; (2) *w/c*: water-to-cement ratio; (3) *a/c*: aggregate-to-cement ratio; (4) *c_type*: cement type; (5) *T*: environmental temperature; (6) *RH*: environmental relative humidity; (7) t_c: time of curing, indicating the start of drying shrinkage; (8) *a_type*: aggregate type. Note that parameters *c_type* and *a_type* are sparse categorical parameters that will be specified in Section 3.3. The parameter *VS* is the notational size of the specimen. Based on the formula of MC 2010 (fib, 2013), the notational size of the dog-bone specimen used in the TCM model is calculated as 85.7 mm, according to the geometry of the TSTM test specimen (Liang, Li, et al., 2022; Lokhorst, 2001).

3.1 | Adjusted MC 2010

This paper keeps most of the formulas of MC 2010 (fib, 2013), except for an adjustment in the drying shrinkage calculation. In the MC 2010, drying shrinkage is calculated as

$$\varepsilon_{ds}\ (t,t_c) = \varepsilon_{ds0}\ (f_{c28})\,\beta_{RH}\,(RH)\,\beta_{ds}\,(t-t_c) \tag{17}$$

where ε_{ds0} is the asymptotic value of drying shrinkage, depending on the 28-day compressive strength f_{c28}; β_{RH} is the coefficient for the effects of relative humidity; β_{ds} is the coefficient for the effects of drying time. However, Equation (17) neglects the evolving effects of drying shrinkage, by assuming the same drying shrinkage evolution even though the time of curing t_c may be different. It is clear that drying shrinkage starting from different ages is different: with longer curing time, drying shrinkage starts at a more mature age and can be much lower (Bal & Buyle-Bodin, 2013; Yang et al., 2017). In the TCM model, this would result in a jump in the EAS curve at the end of curing time. Thereby, in this study, an aging coefficient term is added to Equation (17) to complement this effect:

$$\varepsilon_{ds}\ (t,t_c) = \varepsilon_{ds0}\ (f_{c28})\,\beta_{tc}\,(t_c)\,\beta_{RH}\,(RH)\,\beta_{ds}\,(t-t_c) \tag{18a}$$

$$\beta_{tc}\ (t_c) = \exp\left(1-\left(\frac{t_c}{3}\right)^{0.21}\right) \tag{18b}$$

where β_{tc} is the aging term, depending on the curing of time. The aging term of Equation (18b) results in an exponential decay of drying shrinkage as the curing time increases. Note that the coefficients of Equation (18b) are fitted by the results of (Bal & Buyle-Bodin, 2013) and are only used tentatively in this study to account for the aging effects of drying shrinkage. For a solid conclusion about the aging pattern of drying shrinkage, additional experiments should be performed.

3.2 | XGBoost model for compressive strength

Another important module of this material model is the XGBoost model for predicting the compressive strength, which is a significant input for the MC 2010. A number of studies on compressive strength prediction based on mix parameters have validated the advantages of XGBoost model over many other machine learning models and standard codes (Wan et al., 2021). Based on the database of Northwestern University (Hubler et al., 2015), an XGBoost model was created herein to predict the 28-day compressive strength of concrete, based on mixture proportions, including cement amount, water–cement ratio, aggregate-cement ratio, and cement type (Chen & Guestrin, 2016). The database contains 2606 data of compressive strength and is open-source. Based on a total number of 490 decision trees, the XGBoost model is trained based on 1825 samples with a learning rate of 0.1712. As shown in Figure 6, with 1825 samples in the training set, the coefficient of determination (R^2) over 781 unseen samples is 0.94. High accuracy in the testing set indicates the effectiveness of the XGBoost and the hyperparameter settings. Before XGBoost is incorporated into the material model, it is trained with the whole dataset to ensure the best prediction accuracy. It should be noted that typically 8–12 features are used in the prediction of compressive strength. However, only the four most influential parameters are used as features of the XGBoost model. This is done to remain consistent with the MC 2010 model and can to some extent sacrifice the applicability of the XGBoost model.

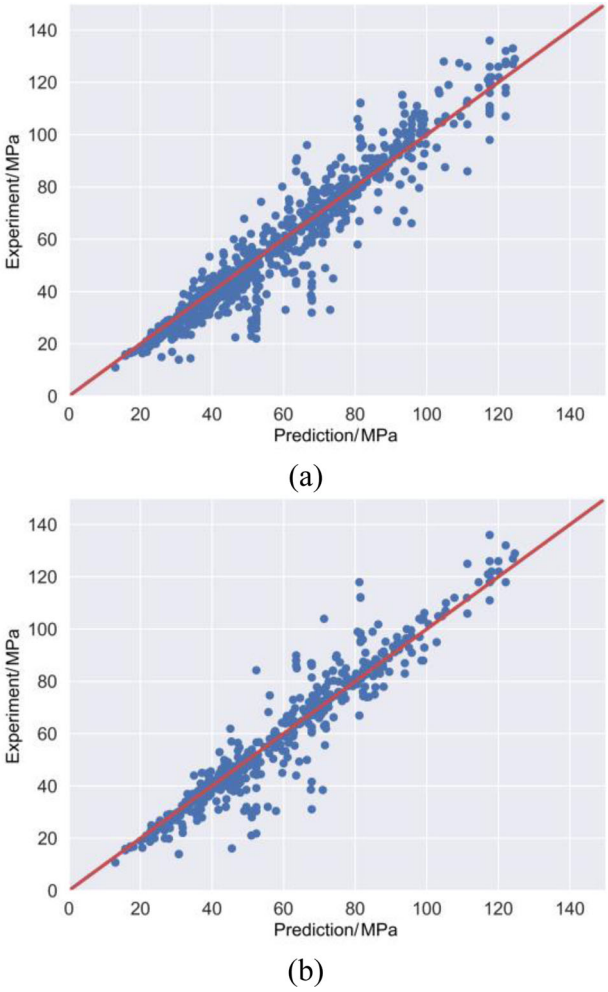

FIGURE 6 Cross-validation results of the eXtreme Gradient Boosting (XGBoost) model of compressive strength: (a) training set, 1825 samples, $R^2 = 0.9837$; (b) testing set, 781 samples, $R^2 = 0.9443$

TABLE 1 Parameter settings of the TCM model

Thermo-field (Equations 4 and 5)	
Thermal conductivity (W/(m*K))	2.3
Heat capacity (J/ (kg*K))	1100
Heat transfer coefficient (W/(m2*K))	2.5
Ultimate hydration heat (J/g)	400, 439, 520
Chemo-field (Equations 1 and 3)	
Fitting parameter A_1	1.41×10^7, 4×10^7, 8×10^7
Fitting parameter A_2	1×10^{-2}, 5×10^{-2}, 8×10^{-2}
Fitting parameter η	8, 8.5, 8
Ultimate hydration degree	$1.031\times wc/(0.194+wc)$
Activation energy/R (K)	5000, 5292, $5490+1470\times(20\text{-}T)$
Mechanical-field (Equations 10 and 12)	
Compressive strength f_c (MPa)	XGBoost (*w/c, a/c, c, c_type, T*)
Shrinkage ε_{sh}	MC2010 (f_c, t_c, *RH, T*)
Elastic modulus E (GPa)	MC2010 (f_c, *a_type, T*)
Creep compliance J (Mpa^{-1})	MC2010 (f_c, *E, RH, T*)

TABLE 2 Categorical parameter settings

Cement type	
c_type = 1	*32.5N*
c_type = 2	*32.5R and 42.5 N*
c_type = 3	*42.5R, 52.5N, 52.5R*
Aggregate type	
a_type = 1	Basalt or limestone aggregates
a_type = 2	Quartzite aggregates
a_type = 3	Limestone aggregates
a_type = 4	Sandstone aggregates

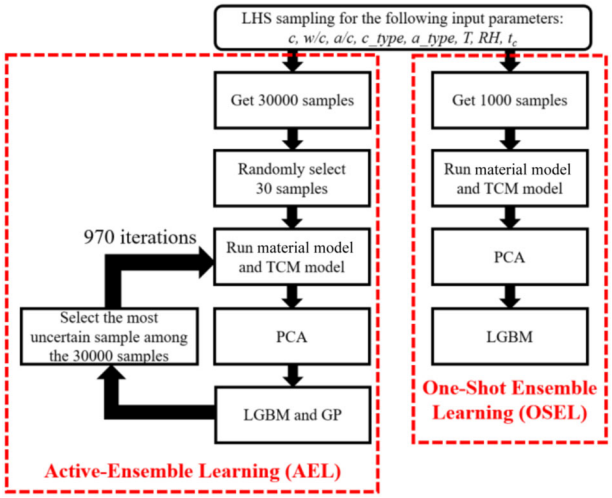

FIGURE 7 Machine learning workflow of this paper

3.3 | Parameter settings

The parameters used in the TCM model are given in Table 1. In the thermo-field, constant values are assumed for thermal conductivity and heat capacity of concrete (Batog & Giergiczny, 2017). The heat transfer coefficient is also taken as constant, assuming a curing measure of "curing blanket and plastic sheet" according to (Lee et al., 2009). Parameters A_1, A_2, and η are material parameters controlling the chemical affinity and hydration degree in Equation (1). A_1, A_2, and η can be obtained by fitting the temperature rise in an adiabatic test (Cervera et al., 1999a). For the parameter *ultimate hydration heat* and fitting parameters A_1, A_2, and η, three different values are assumed for each parameter to characterize different cement types *c_type* (di Luzio & Cusatis, 2009a, 2009b). Furthermore, four aggregate types are contained in the parameter *a_type*. The categorical parameter settings for cement type and aggregate type are shown in Table 2. The specific values for these parameters are determined by referring to published multifield models and the thermal properties of concrete (di Luzio & Cusatis, 2009a, 2009b; Klemczak et al., 2018). Note that the parameters settings are only used to set up the framework for parametric analysis of the TCM model and serve as the database for building the AEL model. For practical use, the parameter settings should be first validated through a rigorous experimental procedure.

4 | AEL MODEL

The machine learning workflow of this paper is shown in Figure 7, with the left branch being the AEL and the right being the OSEL. Both learning frameworks follow a similar technical route: (1) LHS is first conducted to obtain the sample space; (2) the material model (see Section 3) and the TCM model (see Section 2) are run based on the selected samples; (3) PCA is conducted to process the EAS vector; (4) a multi-output LGBM is trained.

A major difference between AEL and OSEL lies in the sampling method during the training stage. For OSEL, there is only one-shot sampling by the LHS method, which will be iteratively solved by the TCM model and used to train the LGBM model. For the AEL, a two-stage sampling strategy is adopted: (1) the first 30 samples are initially used to build a GP model and LGBM model; (2) the GP model is updated iteratively using all observed samples, and then, based on Bayesian inference, the variance distribution of

the GP over the whole 30000-sample pool is calculated; the sample point with the highest variance is considered as the most uncertain sample in this study. This new sample is imported to the TCM model and the result is then used to update the GP model and the LGBM model. Such active learning method intentionally pays more attention to exploring uncertain samples and uses these samples to update the LGBM model. The AEL model runs 970 iterations to gain another 970 samples, which ensures the same number of total samples for training the LGBM with the OSEL method. Therefore, the effectiveness of AEL and OSEL can be compared.

4.1 | Data sampling and preprocessing

4.1.1 | LHS

To construct the database for machine learning, a sample pool is needed first. Monte Carlo sampling is a frequently used approach, which is often based on a pseudorandom number generator and a known transformation to randomly generate samples for each variable. However, an unavoidable drawback is that many samples are required for good accuracy and repeatability of a certain probabilistic distribution. In comparison, LHS achieves a better representation of the interested probabilistic distribution using a smaller number of samples (Loh, 1996). The LHS is conducted in the following two steps: (1) Samples for each variable are strategically chosen to represent the variable's probability density function; (2) samples for the variables are ordered to match a certain target (e.g., correlations) between variables.

In this paper, each sample is represented by eight variables, given in Table 3. The range of each variable is specified to (1) represent most general cases of concrete structures and (2) conform to the applicability range of the MC 2010. At first, all the variables are assumed as independent and uniformly distributed to generate an initial database. Afterward, two measures are taken to process the database: (1) the values of aggregate type and cement type are rounded down to obtain integers that represent categorical parameters as shown in Table 2; (2) according to practical engineering experience, the w/c of lower strength cement (i.e., $c\_type = 1$) should not be lower than 0.4. Therefore, the samples with a c_type equal to 1 and w/c smaller than 0.4 are deleted from the initial database.

In the LHS process, based on the criterion of maximizing the minimum distance between sample points, five iterations are used to generate the sample pool. As a result, the one-shot training set for the OSEL learning is shown in Figure 8.

TABLE 3 Variables range of the samples

Variable name	Variable range
Temperature T (°C)	0~40
Relative humidity RH (%)	40~100
Time of curing t_c (hours)	12~672
Aggregate-cement ratio a/c (1)	2~8
Water–cement ratio w/c (1)	0.2~0.6
Cement amount c (kg/m^3)	250~650
Aggregate type a_type (1)	Four kinds: 1, 2 , 3, 4
Cement type c_type (1)	Three kinds: 1, 2, 3

4.1.2 | PCA

After the sample pools are ready, the samples can be imported to the TCM model and run the EAS simulation. The EAS result of each sample is a 672-by-1 vector, which represents the restraint stress from the first to 672th hour. Such a long vector can be an issue for ML models. To address this problem, PCA is used to reduce the dimensionality of the EAS vector, before it is used for training. By singular value decomposition (Halko et al., 2011), PCA conducts linear dimensionality reduction of the data by projecting it to a lower dimensional space. In this paper, the general process of PCA can be described as follows:

$$\sigma_{PCA} = U\sigma_{original} \tag{19}$$

where $\sigma_{original}$ is the 672-by-1 EAS vector output by the TCM model; σ_{PCA} is the 5-by-1 principal component (PC) vector produced by PCA to represent the 672-by-1 EAS vector; U is a 5-by-672 matrix, which represents the new basis to project $\sigma_{original}$ to σ_{PCA}. U is composed of the first 5 eigenvectors of the covariance matrix of $[\sigma_{original}]_N$ (i.e., $(1/N)$ $[\sigma_{original}]_N$ $[\sigma_{original}]_N{}^T$), N is the number of samples that are used in PCA), ordered by their variance (i.e., eigenvalues). For OSEL, PCA can be conducted at once based on 1000 randomly selected samples. For AEL, which conducts a progressive sampling procedure, PCA is first applied to the 30 initial samples and then restarted in every learning step to take new samples into account.

Note that the reason why 5 eigenvectors are chosen is due to the variance ratio distribution of PCs as shown

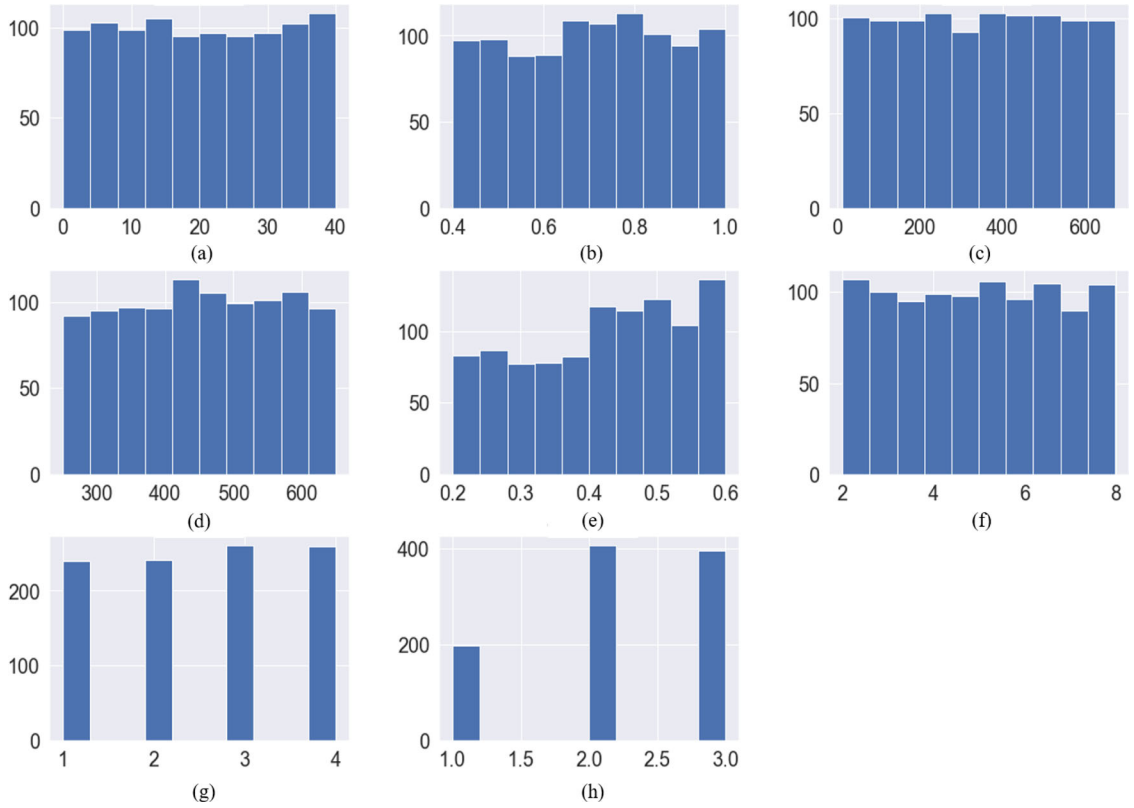

FIGURE 8 Latin hypercube sampling (LHS) sampling for one-shot ensemble learning (OSEL): (a) temperature (°C); (b) relative humidity (%); (c) time of curing (hours); (d) cement amount (kg/m^3); (e) w/c ratio; (f) a/c ratio; (g) aggregate type; (h) cement type. The Y-axes present the number of samples

TABLE 4 Variance ratios of the principal components (PCs)

PC rank	Variance ratio
FirstPC	9.8637×10^{-1}
Second PC	1.1917×10^{-2}
Third PC	8.9869×10^{-4}
Fourth PC	3.6584×10^{-4}
Fifth PC	1.6026×10^{-4}

in Table 4. It is found that the first 5 PCs already occupy almost 100% variance, and the first PC has already explained over 98% variance of the original EAS, which indicates a strong linearity of the original EAS vector in the projected space of PCA.

Nine cases are randomly selected to compare the original EAS vector and the corresponding PCA processed vector as shown in Figure 9. The comparison shows a near-perfect match between these two kinds of vectors. The mean squared error (MSE) between these two kinds of vectors is computed over the whole sample pool, and a value of 0.0005618 MPa is obtained. Such a low MSE validates that the PCA can effectively reduce the dimensionality of the EAS vector from 672-by-1 to 5-by-1 while maintaining the majority of the information.

With the samples obtained by LHS and corresponding EAS results processed by PCA, the training data for machine learning approach are prepared. After a normalization procedure by the mean and variance of the data, the dataset can be imported to machine learning models to start the training process.

4.2 | Uncertainty-based query: GP

The number of labeled samples is essential for the generalization capabilities of Machine Learning (ML) models. However, obtaining a large amount of labeled data from the TCM model is computationally expansive. In this regard, this paper adopts the uncertainty-based query to actively select samples and run the corresponding TCM model to obtain labeled data, which has a higher potential of improving the performance of the ML model. The GP, which defines a stochastic process that any finite collection of random variables follows a multivariate Gaussian distribution, is adopted to quantify the uncertainty. Inheriting the properties of Gaussian distribution, GP can explicitly describe the marginalized distribution of any unobserved samples, which directly provides a measurement of the uncertainty.

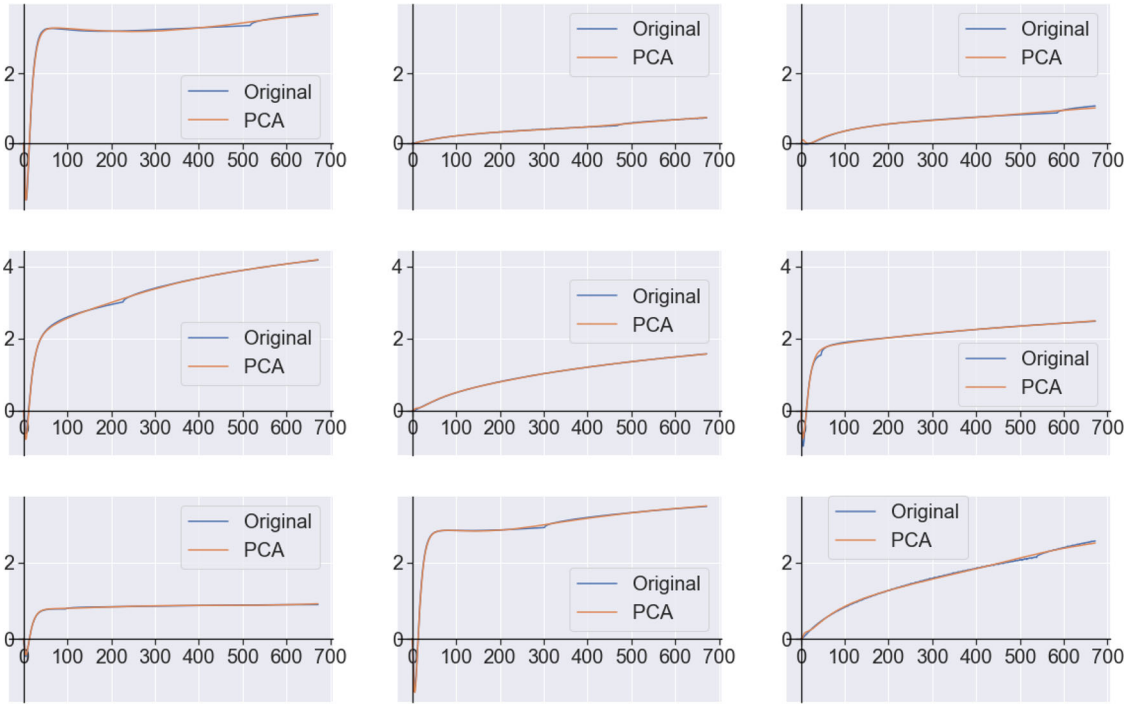

FIGURE 9 Random cases for comparing PCA and original EAS vector. X-axes represent the time (hours). The Y-axes represent stress (MPa).

Assuming having observed samples (***X***,***Y***), a GP (denoted by $f(x)$) is described by a mean and a covariance matrix of observed samples, that is, $f(\boldsymbol{x})\sim GP(\boldsymbol{\mu(X)}, \boldsymbol{k(X,X)})$. By normalizing all the samples with their mean and variance, the $\mu(X)$ can be set as 0. Therefore, the only key component defining the GP turns out to be the covariance matrix $\boldsymbol{k(X,X)}$, which is assembled by the covariance of any two observed samples and is also known as the kernel of GP. The selection criterion of the GP kernel is based on the requirement of smoothness and anticipated patterns of the data (Rasmussen & Williams, 2006). Herein, the radial basis function is chosen as the kernel function, which is infinitely differentiable and therefore can result in good smoothness expressed as

$$k(x_s, x_t) = \sigma^2 \exp\left(\frac{\|x_s - x_t\|^2}{2l^2}\right) \tag{20}$$

where σ and l are hyperparameters to be tuned; $\boldsymbol{x_s}$ and $\boldsymbol{x_t}$ are two observed samples. Equation (20) shows that the GP considers the dependence of any two samples according to their Euclidean distance.

Based on the observed samples, GP makes a prediction on other unobserved samples using Bayesian Inference. Assuming unobserved samples at $\boldsymbol{X^*}$, the joint distribution can be expressed as

$$\begin{bmatrix} Y \\ f(X^*) \end{bmatrix} \sim GP\left(\begin{bmatrix} \mu(X) \\ \mu(X^*) \end{bmatrix}, \begin{bmatrix} k(X,X) & k(X,X^*) \\ k(X^*,X) & k(X^*,X^*) \end{bmatrix}\right) \tag{21a}$$

$$(X,X) = \begin{bmatrix} k(x_1,x_1) & \cdots & k(x_1,x_n) \\ \vdots & \ddots & \vdots \\ k(x_n,x_1) & \cdots & k(x_n,x_n) \end{bmatrix} \tag{21b}$$

$$k(X^*,X) = \begin{bmatrix} k(x^*,x_1)\, k(x^*,x_2) \cdots k(x^*,x_n) \end{bmatrix} \tag{21c}$$

By Bayesian Inference, the marginalized distribution of the unknown sample at $\boldsymbol{X^*}$ can be expressed as (Rasmussen & Williams, 2006):

$$f(X^*)\,|Y \sim GP(\mu^*, k^*) \tag{22a}$$

$$\mu^* = k(X^*,X)\,k(X,X)^{-1}(Y - \mu(X)) + \mu(X^*) \tag{22b}$$

$$k^* = k(X^*,X^*) - k(X^*,X)\,k(X,X)^{-1}k(X,X^*) \tag{22c}$$

where k^* denotes the variance of prediction of GP for the unobserved sample $\boldsymbol{X^*}$. Based on the marginalized

distribution described by Equation (22), a series of learning functions can be defined for the sample query. For example, in the studies of structural reliability, learning functions like the EFF function (Bichon et al., 2008) and the U function (Echard et al., 2011) are often defined to evaluate which samples should be selected in the next learning iteration. These learning functions are built to achieve the exploitation–exploration tradeoff: (1) "exploitation" means that samples located near the limit state will be preferred; (2) "exploration" means that samples with high uncertainty will be preferred. The exploitation–exploration tradeoff guarantees that a surrogate model for reliability analysis can be obtained to achieve high accuracy within only dozens of learning iterations (Tomar & Burton, 2021; Yuan et al., 2022). However, as this paper aims to predict the EAS evolution over a certain time range (0~672 h), the main problem is a global prediction rather than a local prediction that only focuses on a certain boundary (i.e., a limit state). Therefore, in this paper, there is no tradeoff between exploitation and exploration but only greedy exploration for samples with the highest uncertainty. Specifically, in every learning step, Equation (22) is performed over the whole sample pool of the AEL (i.e., 30,000 samples) to obtain the variance distribution. The sample with the highest variance calculated by Equation (22c) will be selected for the next learning process. The variance distribution at some learning steps will be given in Section 5.3.

4.3 | Light Gradient Boosting Machine (LGBM)

The LGBM is used as a prediction model due to its robustness, excellent generalizing capability, and efficiency. The base model used for LGBM is the decision tree, the so-called weak learner. For regression aims, the decision tree consistently makes binary partitions of each variable of the sample at each level of the tree, until the maximum depth is reached (Myles et al., 2004). Therefore, the whole dataset will be divided into multiple regions, with each region corresponding to a certain prediction value. However, one significant drawback of the decision tree is the high risk of overfitting. Due to the hierarchical training process, the error induced at the top levels of a decision tree can be easily propagated down. This makes the decision tree a high-variance model, and a slight change in input data can greatly change the output (Myles et al., 2004).

The ensemble learning method like "bagging" or "gradient boosting" aims to combine a number of decision trees into a strong prediction model. In this paper, the gradient boosting framework is adopted as shown in Figure 10. Starting from a weak learner, the LGBM sequentially builds weak learners to compensate for the residual error

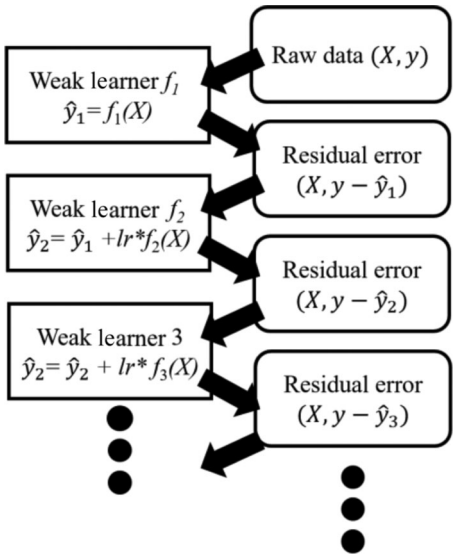

FIGURE 10 Gradient boosting workflow

of previous models and finally assembles all these models to form a final model. Such residual error is the so-called gradient, making this method analog to gradient descent. During this process, the hyperparameter "learning rate" is set as 0.1 to control the step size. To account for the risk of overfitting, a regularization term will be used in the loss function to put preference on a model with lower complexity while preserving high accuracy. Furthermore, a random selection of features and bagging will also be adopted.

Compared to another well-known gradient boosting model—XGBoost, the LGBM shows higher efficiency, which makes it a better choice for the AEL process in this paper. The advantage of LGBM is due to the following three aspects (Ke et al., 2017):

1. Rather than splitting the leaf node of the base model level-wise, LGBM grows the tree leaf-wise using a histogram-based algorithm, which yields high efficiency and saves memory.
2. LGBM adopts gradient-based one-side sampling to select samples with high gradient and discards the ones with low gradient, to reduce sample numbers and increase efficiency.
3. LGBM adopts exclusive feature bundling to identify exclusive features and then merge them into feature bundles to reduce the dimensionality of sample features and thus promote training efficiency.

As an iterative learning process, the high efficiency and accuracy of LGBM are essential for the AEL framework proposed herein. To efficiently tune the hyperparameters of the LGBM model, Bayesian optimization is conducted based on an acquisition function of expected

TABLE 5 Hyperparameter settings for the light gradient boosting machine (LGBM) model

Hyperparameter	Value
Max_bin	76
Min_data_in_leaf	12
Max_depth	62
Num_leaves	38
Feature_fraction	0.883
Bagging fraction	0.773
Num_estimators	100

improvement, which guarantees fast convergence within 30 iterations. A detailed description of the tuning process can be found in the authors' previous work (Liang, Chang et al., 2022). The results of hyperparameters tuning are given in Table 5. The hyperparameter "*Max_bin*" controls the number of bins when conducting the histogram-based algorithm to find the optimal split in each decision tree; the parameters "*Min_data_in_leaf*," "*Max_depth*," "*Num_leaves*" specify the size of each decision tree to prevent overfitting; the parameters "*Feature_fraction*," "*Bagging fraction*," and "*Num_estimators*" control the bagging and boosting process by specifying the fraction of features, the number of samples, and the number of decision trees to be used in the training process. For more details regarding how these parameters influence the performance of LGBM, the reader is referred to Ke et al. (2017).

5 | RESULTS AND DISCUSSION

5.1 | Applicability of the TCM model

5.1.1 | Comparison with testing results

This section presents a comparison with testing results to show the applicability of the TCM model. The experimental TSTM tests conducted by the authors are used here (Liang et al., 2022). It should be noted that there are some differences between the TSTM tests performed and the TCM model:

1. The thermal boundary is different: The TSTM tests were conducted under strictly regulated temperature control at the center of the specimen by water circulation so that there was no thermal deformation induced by cement hydration. In the TCM model, for the sake of generality, the thermal deformation induced by cement hydration and heat transfer are both considered.
2. The material model is different: In the TSTM tests, high-volume slag-blended concrete was used, which displayed a high autogenous expansion at first hours and higher autogenous shrinkage than ordinary concrete described by the MC 2010.

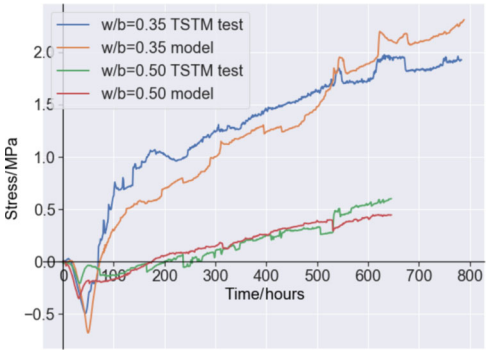

FIGURE 11 Comparison between TSTM tests and modeling results

As described in Section 2, the thermo- and chemo-fields are mainly used to simulate the hydration process and heat transfer, and then relevant material properties and behavior can be derived from the MC 2010 to start the mechanical-field analysis. However, in view of the difference in the thermal boundary and the material model, it is not reasonable to directly run the TCM model built in this paper to simulate the TSTM tests. In this regard, the material behavior and properties of the high-volume slag-blended concrete used in the TSTM tests were tested and directly imported to the mechanical field of the TCM model to run the viscoelastic analysis.

A comparison between the TSTM tests and the modeling results is shown in Figure 11. The results show that, given the right input of material properties and behavior, the viscoelastic mechanical field of the TCM model can still simulate the stress development of TSTM tests with good precision with a root MSE of 0.22 and 0.08 MPa, even though the experimental data are not smooth. The thermo- and chemo-fields of the TCM model, which are based on well-known Fourier's law and Arrhenius equations, have been widely used and validated in studies concerning various early-age behavior of concrete. Therefore, they are considered valid theoretical approaches. Interested readers are referred to the benchmark studies (Cervera et al., 1999a, 1999b; di Luzio & Cusatis, 2009a, 2009b; Gawin et al., 2006a, 2006b).

However, a relevant concern of the TCM model lies in the material model. The authors acknowledge that the material model (MC 2010) adopted here is only valid for common concretes and is probably not suitable for every mix. Development of a material model that covers a wide range of mixes and environmental conditions requires much more advanced and thorough experimentation. Note that the development of such a material model does not

TABLE 6 Details of the input for case study

Input variable	Value
Cement amount c (kg/m^3)	320
Relative humidity *RH* (%)	100
Water–cement ratio *w/c* (1)	0.42
Aggregate-cement ratio *a/c* (1)	5.76
Temperature *T* (°C)	0~40
Time of curing t_c (hours)	672
Aggregate type *a_type* (1)	3
Cement type *c_type* (1)	2

change the basic approach of the TCM-based AEL method, and therefore is not in the scope of this study.

5.1.2 | Case studies

Five representative cases are selected as input to run the proposed TCM model. The input for the case study is given in Table 6. In these five cases, the EAS evolution under different temperatures, ranging from 0 to 40°C, is investigated. By setting the time of curing t_c as 672 h, the autogenous shrinkage-induced EAS is calculated.

The results of the EAS evolution of the five-case study are shown in Figure 12a. Note that the stress value is the surface average at the middle section of the dog-bone specimen. The evolving concrete properties and behaviors, which together determine the EAS development, are also shown in Figure 12b–g, including incremental creep strain (Equation 12d), autogenous shrinkage, effective elastic modulus (Equation 12a), specimen temperature, equivalent age (Equation 7), and tensile strength. Note that, here, "incremental creep strain" is the internal state variable that stores the incremental strain history of the mechanical-field model, computed by Equation (12d). The equivalent age is calculated based on the "maturity concept" (Equation 7), which takes the influence of temperature history on hydration speed into account. These results show that the TCM model can correctly simulate multiple effects related to EAS evolution:

1. Figure 12f shows the influence of temperature on the rate of hydration, which then influences the development of elastic modulus, tensile strength, creep compliance, and autogenous shrinkage (see Figure 12b–d,g). High temperature accelerates the hydration and therefore accelerates the development of all these properties, which finally causes much higher EAS (Lura et al., 2001; Maruyama & Lura, 2019).
2. Figure 12b shows that the magnitude of incremental creep strain decreases monotonically due to the effect of hydration. Negative and positive creep strains correspond to the appearance of compressive and tensile EAS, respectively.
3. Figure 12e shows that higher environmental temperature results in a higher temperature increase in the specimen, and therefore causes higher compressive EAS in the first hours. On the other hand, low temperature can increase the activation energy (Equation 3), slow down the hydration reaction, and also cause rapid loss of heat (Equation 4c). As a result, the temperature in the specimen can hardly change, and there is no compressive EAS in the first hours (Lura et al., 2001).
4. Figure 12d,g shows that the temperature increase simply accelerates the development of elastic modulus and tensile strength in the first days but compromises them at 28 days. This is because high temperature negatively influences the hydration process (Kim et al., 1998). In the TCM model, this effect is originally considered by the MC 2010 formulas.

5.2 | Data correlation

This section investigates the meaning of the first PC and then presents the correlation between the first five PCs and the input parameters. The PCA procedure described in the Section 4.1.2 shows that the first five PCs can express the original EAS vector produced by the TCM model with high accuracy (with an MSE lower than 0.0005618). Moreover, the first PC occupies over 98% of the variance ratio and can be considered a significant variable that represents the EAS vector. However, although the PCA procedure has a clear mathematical meaning, what the first PC exactly represents is unknown a priori. To this end, this study conducts a parametric study on the first PC. First, this study assumes the first PC equals 0, 1, 2, 3, …, 100, and conducts an inverse PCA (inverse of Equation 19) to transform this first PC into a 672-by-1 EAS vector. Note that all 101 sets of inverse PCA are in good order as shown in Figure 13, but only six results are selected to show here to make the pattern clearer and more intuitive.

The results show that the first PC represents the global magnitude of the whole EAS vector, irrespective of whether the specimen is in compression or in tension. Compared with other indexes like "zero-stress temperature" (Dabarera et al., 2022), "peak of compressive stress"

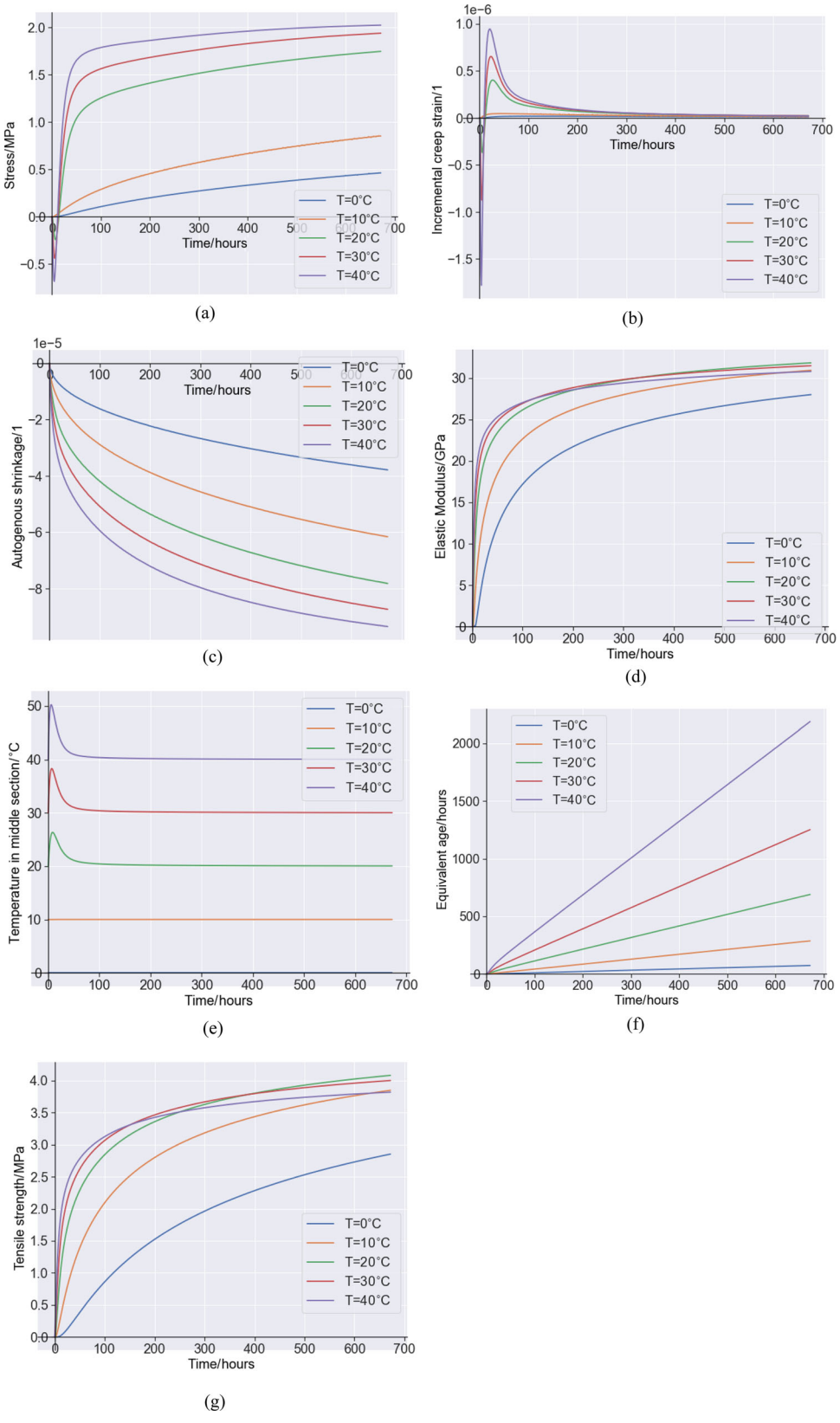

FIGURE 12 Case study of the TCM model: (a) early-age stress (EAS) evolution; (b) incremental creep strain –xx component; (c) autogenous shrinkage; (d) effective elastic modulus; (e) temperature development in specimen; (f) equivalent age; (g) tensile strength

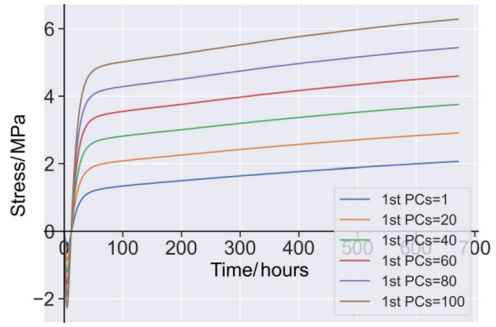

FIGURE 13 Inverse PCA transform of first PC varying from 0 to 100

FIGURE 14 Correlation matrix between PCs and input variables

(Bentz et al., 2008), and "peak of tensile stress" (Shen et al., 2019), which are mostly based on a single observation at a single time point, the first PC represents an overall characteristic of the whole EAS vector and can be regarded as a global index for evaluating the EAS evolution.

Figure 14 shows the correlation matrix between the first five PCs and the input parameters calculated over the 1000 samples of the OSEL. As described before, the first PC occupies the 98% variance ratio among all PCs and represents the global magnitude of the EAS vector. Therefore, the correlation between the first PC and input parameters can reveal the influence of various factors on the EAS evolution. The first row of the correlation matrix stands for the correlation between the first PC and the input parameters. A positive correlation coefficient means that increase of the corresponding parameter can increase the first PC, which means that it increases the overall EAS magnitude. In other words, the corresponding parameter has a positive contribution to the EAS evolution. By analyzing the correlations at the first row of the correlation matrix, the following is observed:

1. Environmental temperature has the highest positive contribution to the EAS evolution, which is not surprising since temperature not only influences the hydration speed but also accounts for a higher heat release in the first hours. Fast hydration accelerates the development of shrinkage and elastic modulus and finally accelerates the EAS evolution as shown in Section 5.1.2. High heat release increases the thermal deformation and can greatly increase both the compressive and the tensile stress.
2. Parameters "cement amount" and "cement type" also have positive contributions to the EAS evolution. High cement amount and cement type indicate more heat release, which can increase EAS. Note that cement types 1, 2, and 3 represent cement class ranging from low strength/slow hydration to high strength/rapid hydration.
3. Parameters w/c ratio, a/c ratio, and aggregate type all have a negative contribution to the EAS evolution. This is in accordance with the common understanding of the physical process: Increasing w/c and aggregate type can result in concrete with lower strength and lower elastic modulus, and therefore slow down the EAS evolution. Although the increase of w/c may result in more drying shrinkage after the curing, the contribution of w/c to EAS magnitude remains negative because the decrease of elastic modulus and autogenous shrinkage plays a more significant role in this process. Increasing the a/c can reduce the amount of cement paste, which is the shrinking phase, and increase the extent of internal restraint, which causes a further decrease in the overall shrinkage.
4. Parameter "time of curing" has a negative contribution since longer curing indicates less drying shrinkage and therefore can cause less EAS.
5. The correlation of RH is low because the influence of RH is complex. According to the material model, increasing RH can result in a decrease in creep and drying shrinkage. Lower creep means lower stress relaxation and therefore higher EAS. However, lower drying shrinkage can reduce EAS, which in fact should also depend on the time of curing. The change of RH can induce counteracting effects among various concrete behaviors so that its influence is not monotonic, at least in the TCM model.

Based on the meaning of the first five PCs and the correlation analysis over 1000 data samples, this section illustrates again that the TCM model proposed in this paper can generate reasonable EAS results given different input parameters.

5.3 | Training history

This section presents the model performance during the learning steps. To evaluate the prediction performance of

the model, this study employs a cross-validation procedure: AEL model will use OSEL's database as a testing set, and OSEL will use AEL's database as a testing set. In this way, both AEL and OSEL have to be tested by 1000 unseen samples. Note that, in machine learning practice, in general, the size of the testing set is 10%–40% of the training set, while this study uses the same size of the training set. In this sense, a big testing set poses a more challenging task for the ML model and can better reflect the model performance.

Mean square error (MSE), mean absolute error (MAE) and coefficient of determination (R^2) are used as the metrics as follows:

$$R^2 = 1 - \frac{\sum_{i=1}^{n} (y_i - \hat{y}_i)^2}{\sum_{i=1}^{n} (y_i - \bar{y})^2} \tag{23}$$

$$RMSE = \frac{1}{n} \sum_{i=1}^{n} (y_i - \hat{y}_i)^2 \tag{24}$$

$$MAE = \frac{1}{n} \sum_{i=1}^{n} |y_i - \hat{y}_i| \tag{25}$$

where y_i is the EAS vector of ith sample point output by the TCM model; $\hat{y}_i$ is the EAS vector predicted by AEL or OSEL model for ith sample; $\bar{y}$ is the mean value of the EAS vector. Note that both AEL and OSEL models give the output of EAS in the form of 5-by-1 PCA component so that an inverse PCA procedure is needed before measuring the performance.

After the training of AEL and OSEL models are finished, a step-by-step analysis is carried out to check their learning history. At each analysis step, the number of samples used for training both models is increased and a cross-validation procedure is conducted as shown in Figure 15. The results show that, as the learning step increases, the number of samples used for training also increases, which improves the performance of both models. AEL outperforms OSEL during the whole training history, irrespective of the metrics used. To achieve a certain accuracy, the number of samples required for AEL is less than 50% of that required for OSEL. For example, the AEL achieves an MSE of 0.125 MPa based on around 200 samples, while for OSEL, achieving the same MSE takes more than 800 samples. This validates the efficiency of the AEL method, which is significant for surrogate modeling for an expansive model like the TCM model.

Although the gap between the AEL and OSEL is stable over the whole training history, it is not very large. The OSEL still obtains good accuracy, with an R^2 close to 0.95 when 1000 samples are used in the training process. Such a good training performance can be attributed to the sample space created by LHS and the robustness of the LGBM model.

The training history shows the advantages of AEL over OSEL. To further consolidate this conclusion and gain a deeper understanding of how AEL works, the final AEL database, which is built by a progressive sampling process guided by uncertainty-based query (see Section 4.2), is shown in Figure 16. Comparing the AEL sampling results with the database of OSEL created by one-shot LHS sampling (see Figure 8), it is found that the AEL sampling puts more attention on the boundaries of the variables, while the OSEL assumes an even-distribution of all the variables and values them equally. The difference can be attributed to the uncertainty-based query in the AEL process, which results in a preference for samples with higher uncertainty (i.e., higher variance). Using the variance of the GP as a measure of uncertainty, the uncertainty-based query continuously looks for the samples with high uncertainty (variance), imports them to run the TCM model, and adds the results to the training set of the LGBM model.

The uncertainty-based query of the AEL results in a consistent change in the distribution of uncertainty (variance) in the sample space at different learning iterations as shown in Figure 17. At 10th learning step, the whole sample space is close to unknown, therefore over 28,000 samples have a variance higher than 0.9, and the other 2000 samples have a variance between 0.8 and 0.9. As the AEL progress, the sample with the highest variance is used to run the TCM model and then train the LGBM and GP. This sampling strategy directly causes a decrease in the maximum variance and a shift in overall variance distribution from high to low value: (1) After 500 learning iterations, the maximum variance decreases to 0.9 from 1, and the variance range shifts to (0.44, 0.90) from (0.7, 1.0); (2) After 970 learning iterations, the maximum variance decreases to 0.76, and the variance range shifts to (0.32, 0.76). The evolution of variance distribution also shows that the decrease of maximum variance and the shift of variance range become slower as the learning iteration increases.

5.4 | Testing

Following the cross-validation described in Section 5.3, in which the AEL model uses OSEL's database as a testing set, and OSEL uses AEL's database as a testing set, the testing results of the AEL and OSEL are shown in Figure 18. The red line is a perfect-prediction line, and the data aligning on the red line mean that the AEL or OSEL prediction (X-axis) is equal to the TCM modeling results (Y-axis). The testing results show that both AEL and OSEL can obtain high R^2 and low MSE and MAE, with the majority of testing samples gathering around the perfect-prediction line.

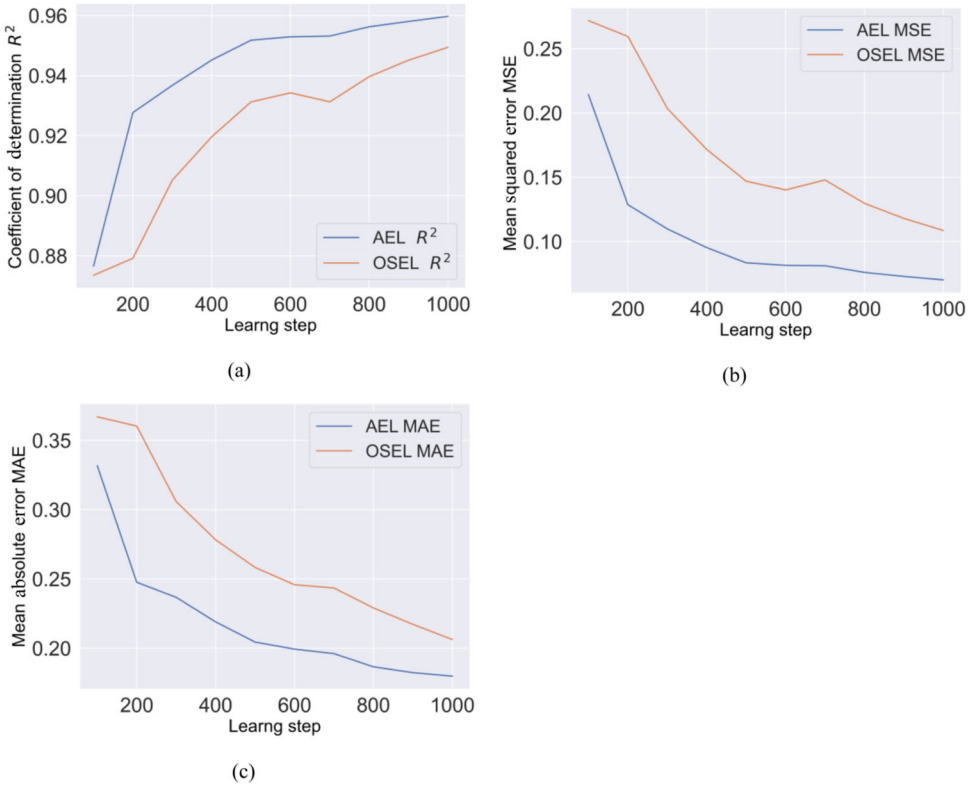

FIGURE 15 Training history of the active ensemble learning (AEL) and OSEL model: (a) coefficient of determination; (b) mean squared error; (c) mean absolute error

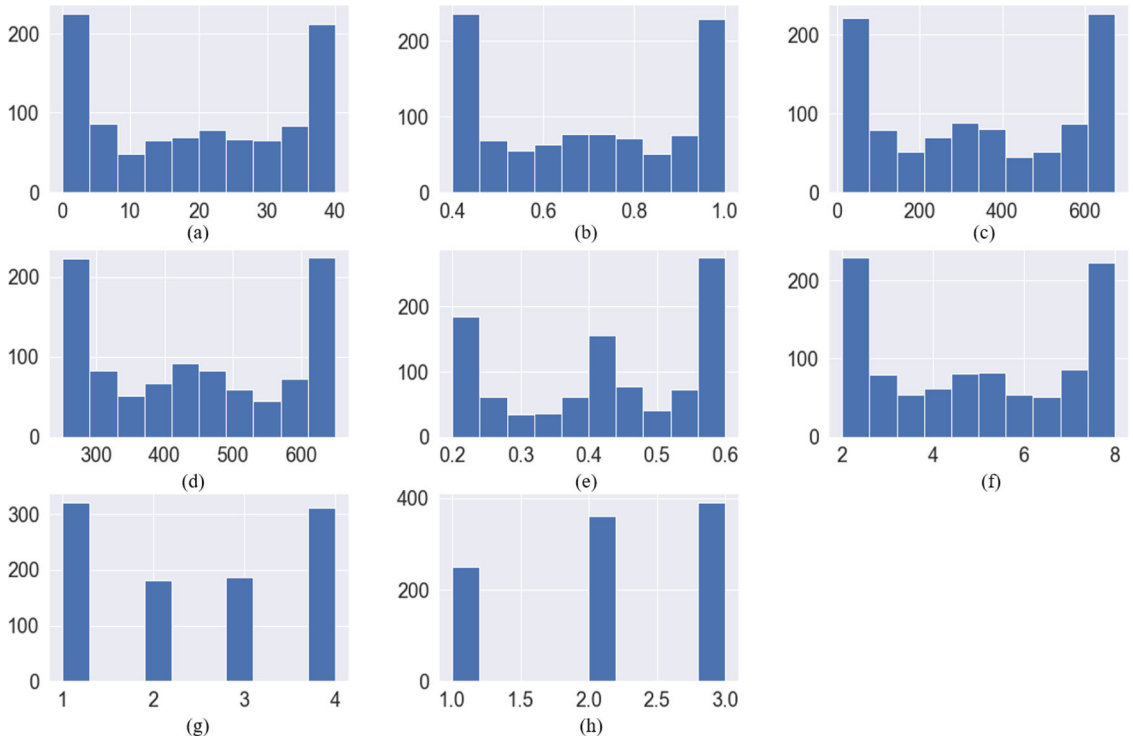

FIGURE 16 AEL sampling results of uncertainty-based query: (a) temperature (°C); (b) relative humidity (%); (c) TIME of curing (hours); (d) cement amount (kg/m^3); (e) w/c ratio; (f) a/c ratio; (g) aggregate type; (h) cement type. The Y-axes presents the number of samples.

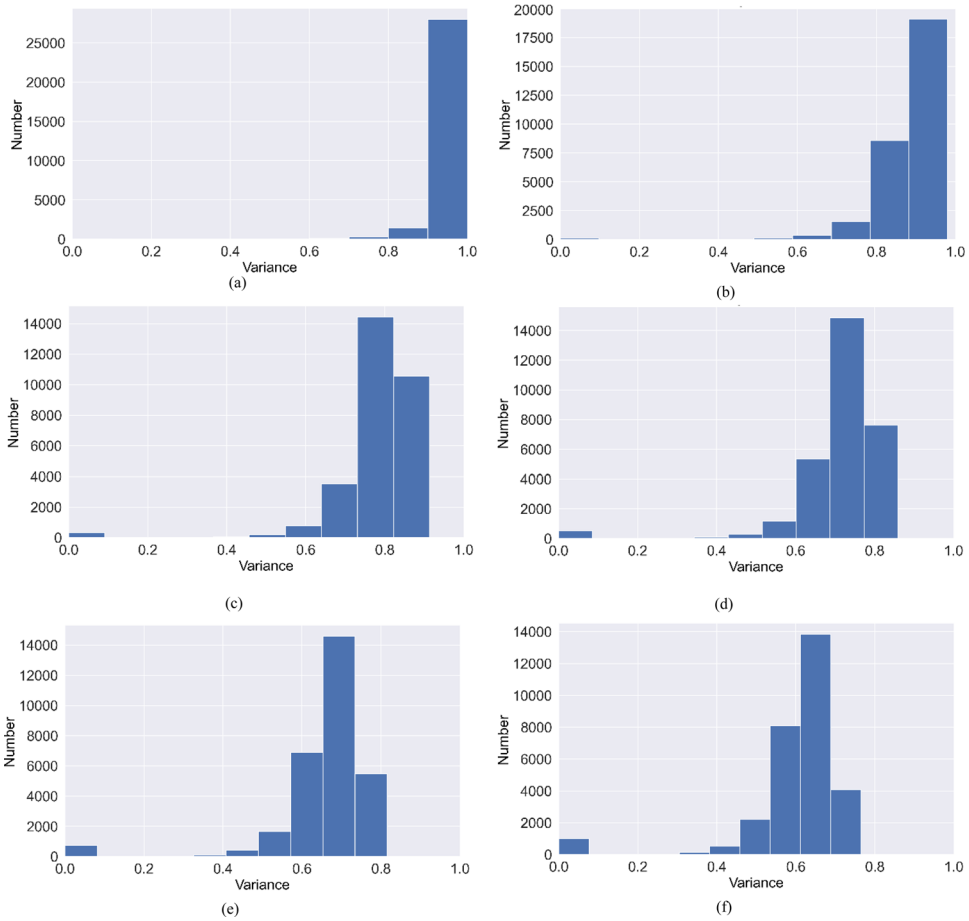

FIGURE 17 Variance histogram at different learning iterations: (a) Step 10; (b) Step 100; (c) Step 300; (d) Step 500; (e) Step 700; and (f) Step 970

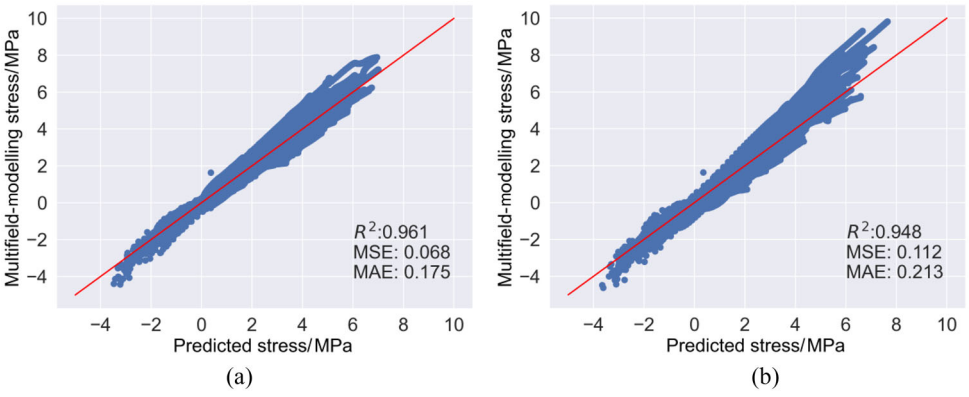

FIGURE 18 Testing results of AEL and OSEL: (a) AEL; (b) OSEL

AEL results show a smaller deviation from the perfect-prediction line, which indicates better performance. This is in accordance with the results of all three metrics as shown in the training history of Section 5.3. More specifically, the OSEL prediction at high-stress conditions shows a significant deviation from the perfect-prediction line, which indicates AEL's advantage at the sample space boundary. This advantage is due to the uncertainty-based query that puts preference in the boundary of sample variables as shown in Figure 16. Although the advantage of AEL over OSEL shown here is obvious, it should also be noted that the cross-validation procedure that uses the AEL's dataset

as OSEL's testing set exposes the weakness of OSEL to a higher extent. Therefore, the advantages of AEL over OSEL shown here may be overestimated.

6 | CONCLUSION

To accurately predict the EAS evolution of concrete, an AEL method is proposed to efficiently construct a surrogate model of a TCM model. Based on the rigorous theoretical basis, the TCM model is built to simulate the aging material properties and behaviors of concrete, which together result in the evolution of EAS under restrained conditions. The AEL framework incorporates PCA, GP, and LGBM. To evaluate the efficiency and precision of the AEL framework, OSEL is also conducted as a comparison. Overall, based on this study, the following conclusions can be drawn:

1. The dimensionality of the EAS vector can be effectively reduced by PCA, with the first PC occupying a variance ratio of over 98%. The parametric study finds that the first PC represents the magnitude of the EAS vector, which means that the first PC can be used as a global index for evaluating the EAS evolution.
2. The comparison between the mechanical modeling results with TSTM tests, the case study, and the correlation analysis for the first PC together prove the applicability of the proposed TCM model. Based on Fourier's law, Arrhenius's equation, rate-type creep law, and the built material model, the TCM model is able to simulate the EAS evolution induced evolving properties (i.e., viscoelasticity) and evolving behaviors (i.e., thermal, autogenous, and drying deformation). By analyzing the results of over 1000 samples, it is found that ambient temperature is the most significant factor that can increase the EAS magnitude. The influence of the other parameters (i.e., w/c, a/c, aggregate type, cement type, cement amount, relative humidity, and time of curing) is also quantified by their correlation coefficients.
3. The AEL framework built in this study outperforms the traditional machine learning routine OSEL with higher R^2 (i.e., 0.961 vs. 0.948), lower MSE (0.068 vs. 0.112), and lower MAE (0.175 vs. 0.213). Based on the uncertainty-based query, the AEL keeps putting attention on the uncertain samples, which are mostly located at the boundary of the sampling space. The active learning process guided by the uncertainty-based query results in consistent improvement of the uncertainty (variance) distribution and greatly improves the prediction accuracy of EAS under extreme conditions.
4. To achieve a certain accuracy, the AEL framework only needs a small sample size, which is less than 50% of the OSEL. This is a great advantage in efficiency because running the TCM model is computationally expansive and obtaining a large dataset through TCM modeling is difficult.
5. The proposed AEL method can effectively build a surrogate of the multi-field model to allow for more efficient optimization and reliability analysis of the structural design to prevent EAC. It is suggested that further improvement concentrates on the learning function of the AEL process, which can achieve more efficient global sampling and prediction.

ACKNOWLEDGMENTS

Minfei Liang and Ze Chang would like to acknowledge the funding supported by China Scholarship Council under Grant Numbers 202007000027 and 201806060129.

REFERENCES

Asteris, P. G., Skentou, A. D., Bardhan, A., Samui, P., & Pilakoutas, K. (2021). Predicting concrete compressive strength using hybrid ensembling of surrogate machine learning models. *Cement and Concrete Research*, *145*, 106449. https://doi.org/10.1016/j.cemconres.2021.106449

Azenha, M., Kanavaris, F., Schlicke, D., Jędrzejewska, A., Benboudjema, F., Honorio, T., Šmilauer, V., Serra, C., Forth, J., Riding, K., Khadka, B., Sousa, C., Briffaut, M., Lacarrière, L., Koenders, E., Kanstad, T., Klausen, A., Torrenti, J. M., & Fairbairn, E. M. R. (2021). Recommendations of RILEM TC 287-CCS: Thermo-chemo-mechanical modelling of massive concrete structures towards cracking risk assessment. *Materials and Structures/Materiaux et Constructions*, *54*(4), 135. https://doi.org/10.1617/s11527-021-01732-8

Bal, L., & Buyle-Bodin, F. (2013). Artificial neural network for predicting drying shrinkage of concrete. *Construction and Building Materials*, *38*, 248–254. https://doi.org/10.1016/J.CONBUILDMAT.2012.08.043

Batog, M., & Giergiczny, Z. (2017). Influence of mass concrete constituents on its properties. *Construction and Building Materials*, *146*, 221–230. https://doi.org/10.1016/j.conbuildmat.2017.04.085

Bayar, G., & Bilir, T. (2019). A novel study for the estimation of crack propagation in concrete using machine learning algorithms. *Construction and Building Materials*, *215*, 670–685. https://doi.org/10.1016/J.CONBUILDMAT.2019.04.227

Bažant, Z. P., & Chern, J. (1985). Strain softening with creep and exponential algorithm. *Journal of Engineering Mechanics*, *111*(3), 391–415. https://doi.org/10.1061/(ASCE)0733-9399(1985)111:3(391)

Bažant, Z. P., & Jirásek, M. (2018). *Creep and hygrothermal effects in concrete structures* (Vol. 225). Springer. https://doi.org/10.1007/978-94-024-1138-6

Bazant, Z. P., & Kaplan, M. F. (1996). *Concrete at high temperatures: Material properties and mathematical models*. Longman Group Limited.

Bazant, Z. P., Xi, Y., & Baweja, S. (1995). Continuous retardation spectrum for solidification theory of aging creep of concrete.

Proceedings of Engineering Mechanics (Part 2), Boulder, CO (pp. 970–973).

Bentz, D. P. (2008). A review of early-age properties of cement-based materials. *Cement and Concrete Research*, *38*(2), 196–204. https://doi.org/10.1016/j.cemconres.2007.09.005

Bentz, D. P., Sant, G., & Weiss, J. (2008). Early-age properties of cement-based materials. I: Influence of cement fineness. *Journal of Materials in Civil Engineering*, *20*(7), 502–508. https://doi.org/10.1061/(ASCE)0899-1561(2008)20:7(502)

Bichon, B. J., Eldred, M. S., Swiler, L. P., Mahadevan, S., & McFarland, J. M. (2008). Efficient global reliability analysis for nonlinear implicit performance functions. *AIAA Journal*, *46*(10), 2459–2468. https://doi.org/10.2514/1.34321

Breiman, L. (1996). Bagging predictors. *Machine Learning*, *24*(2), 123–140. https://doi.org/10.1007/BF00058655

Breiman, L. (2001). Random forests. *Machine Learning*, *45*(1), 5–32. https://doi.org/10.1023/A:1010933404324

Breugel, K. V. (1991). *Simulation of hydration and formation of structure in hardening cement-based materials*. (Doctoral dissertation), Ed.tu Delft (Vol. 02, Issue 7).

Briffaut, M., Benboudjema, F., & D'Aloia, L. (2016). Effect of fibres on early age cracking of concrete tunnel lining. Part I: Laboratory ring test. *Tunnelling and Underground Space Technology*, *59*, 215–220. https://doi.org/10.1016/J.TUST.2016.07.016

Cai, R., Han, T., Liao, W., Huang, J., Li, D., Kumar, A., & Ma, H. (2020). Prediction of surface chloride concentration of marine concrete using ensemble machine learning. *Cement and Concrete Research*, *136*, 106164. https://doi.org/10.1016/j.cemconres.2020.106164

Carol, I., & Bažant, Z. P. (1993). Viscoelasticity with aging caused by solidification of nonaging constituent. *Journal of Engineering Mechanics*, *119*(11), 2252–2269. https://doi.org/10.1061/(ASCE)0733-9399(1993)119:11(2252)

Cervera, M., Oliver, J., & Prato, T. (1999a). Thermo-chemo-mechanical model for concrete. I: Hydration and aging. *Journal of Engineering Mechanics*, *125*(9), 1018–1027. https://doi.org/10.1061/(ASCE)0733-9399(1999)125:9(1018)

Cervera, M., Oliver, J., & Prato, T. (1999b). Thermo-chemo-mechanical model for concrete. II: Damage and creep. *Journal of Engineering Mechanics*, *125*(9), 1028–1039. https://doi.org/10.1061/(ASCE)0733-9399(1999)125:9(1028)

Chu, I., Kwon, S. H., Amin, M. N., & Kim, J. K. (2012). Estimation of temperature effects on autogenous shrinkage of concrete by a new prediction model. *Construction and Building Materials*, *35*, 171–182. https://doi.org/10.1016/j.conbuildmat.2012.03.005

Chen, T., & Guestrin, C. (2016). XGBoost. *Proceedings of the 22nd ACM SIGKDD International Conference on Knowledge Discovery and Data Mining*, San Francisco, CA (pp. 785–794). https://doi.org/10.1145/2939672.2939785

Chiniforush, A. A., Gharehchaei, M., Akbar Nezhad, A., Castel, A., Moghaddam, F., Keyte, L., Hocking, D., & Foster, S. (2022). Numerical simulation of risk mitigation strategies for early-age thermal cracking and DEF in concrete. *Construction and Building Materials*, *322*, 126478. https://doi.org/10.1016/J.CONBUILDMAT.2022.126478

Dabarera, A., Li, L., Lura, P., & Dao, V. (2022). Assessing the zero-stress temperature in high performance concrete at early age. *Cement and Concrete Composites*, *127*, 104384. https://doi.org/10.1016/J.CEMCONCOMP.2021.104384

di Luzio, G., Cedolin, L., & Beltrami, C. (2020). Tridimensional long-term finite element analysis of reinforced concrete structures with rate-type creep approach. *Applied Sciences*, *10*(14), 4772. https://doi.org/10.3390/app10144772

di Luzio, G., & Cusatis, G. (2009a). Hygro-thermo-chemical modeling of high performance concrete. I: Theory. *Cement and Concrete Composites*, *31*(5), 301–308. https://doi.org/10.1016/J.CEMCONCOMP.2009.02.015

di Luzio, G., & Cusatis, G. (2009b). Hygro-thermo-chemical modeling of high-performance concrete. II: Numerical implementation, calibration, and validation. *Cement and Concrete Composites*, *31*(5), 309–324. https://doi.org/10.1016/J.CEMCONCOMP.2009.02.016

di Luzio, G., & Cusatis, G. (2013). Solidification–microprestress–microplane (SMM) theory for concrete at early age: Theory, validation and application. *International Journal of Solids and Structures*, *50*(6), 957–975. https://doi.org/10.1016/J.IJSOLSTR.2012.11.022

De Schutter, G. (2004). Applicability of degree of hydration concept and maturity method for thermo-visco-elastic behaviour of early age concrete. *Cement & Concrete Composites*, *26*(5), 437–443. https://doi.org/10.1016/S0958-9465(03)00067-2

Echard, B., Gayton, N., & Lemaire, M. (2011). AK-MCS: An active learning reliability method combining Kriging and Monte Carlo simulation. *Structural Safety*, *33*(2), 145–154. https://doi.org/10.1016/j.strusafe.2011.01.002

fib. (2013). *fib model code for concrete structures 2010*. Wiley. https://doi.org/10.1002/9783433604090

Gao, Y., Zhang, J., & Han, P. (2013). Determination of stress relaxation parameters of concrete in tension at early-age by ring test. *Construction and Building Materials*, *41*, 152–164. https://doi.org/10.1016/J.CONBUILDMAT.2012.12.004

Gawin, D., Pesavento, F., & Schrefler, B. A. (2006a). Hygro-thermo-chemo-mechanical modelling of concrete at early ages and beyond. Part I: hydration and hygro-thermal phenomena. *International Journal for Numerical Methods in Engineering*, *67*(3), 299–331. https://doi.org/10.1002/nme.1615

Gawin, D., Pesavento, F., & Schrefler, B. A. (2006b). Hygro-thermo-chemo-mechanical modelling of concrete at early ages and beyond. Part II: Shrinkage and creep of concrete. *International Journal for Numerical Methods in Engineering*, *67*(3), 332–363. https://doi.org/10.1002/nme.1636

Gomaa, E., Han, T., ElGawady, M., Huang, J., & Kumar, A. (2021). Machine learning to predict properties of fresh and hardened alkali-activated concrete. *Cement and Concrete Composites*, *115*, 103863. https://doi.org/10.1016/J.CEMCONCOMP.2020.103863

Halko, N., Martinsson, P. G., & Tropp, J. A. (2011). Finding structure with randomness: Probabilistic algorithms for constructing approximate matrix decompositions. *SIAM Review*, *53*(2), 217–288. https://doi.org/10.1137/090771806

Han, T., Siddique, A., Khayat, K., Huang, J., & Kumar, A. (2020). An ensemble machine learning approach for prediction and optimization of modulus of elasticity of recycled aggregate concrete. *Construction and Building Materials*, *244*, 118271. https://doi.org/10.1016/J.CONBUILDMAT.2020.118271

Hansen, F. P., & Pedersen, J. (1977). Maturity computer for controlled curing and hardening of concrete. *Nordisk Betong*, *1*, 19–34.

Hilloulin, B., & Tran, V. Q. (2022). Using machine learning techniques for predicting autogenous shrinkage of concrete incorporating superabsorbent polymers and supplementary cementitious

materials. *Journal of Building Engineering*, *49*, 104086. https://doi.org/10.1016/j.jobe.2022.104086

Hoffman, J. D., Hoffman, J. D., & Frankel, S. (2018). Numerical methods for engineers and scientists. In J. D. Hoffman, & S. Frankel (Eds.), *Numerical methods for engineers and scientists*. CRC Press. https://doi.org/10.1201/9781315274508

Hubler, M. H., Wendner, R., & Bažant, Z. P. (2015). Comprehensive database for concrete creep and shrinkage: Analysis and recommendations for testing and recording. *ACI Materials Journal*, *112*(4), 547–558. https://doi.org/10.14359/51687452

Jeong, S., Murayama, M., & Yamamoto, K. (2005). Efficient optimization design method using Kriging model. *Journal of Aircraft*, *42*(2), 413–420. https://doi.org/10.2514/1.6386

Jones, D. R., Schonlau, M., & Welch, W. J. (1998). Efficient global optimization of expensive black-box functions. *Journal of Global Optimization*, *13*(4), 455–492. https://doi.org/10.1023/A:1008306431147

Kang, F., & Li, J. (2020). Displacement model for concrete dam safety monitoring via Gaussian process regression considering extreme air temperature. *Journal of Structural Engineering*, *146*(1), 05019001. https://doi.org/10.1061/(ASCE)ST.1943-541X.0002467

Kang, M. C., Yoo, D. Y., & Gupta, R. (2021). Machine learning-based prediction for compressive and flexural strengths of steel fiber-reinforced concrete. *Construction and Building Materials*, *266*, 121117. https://doi.org/10.1016/J.CONBUILDMAT.2020.121117

Karbassi, A., Mohebi, B., Rezaee, S., & Lestuzzi, P. (2014). Damage prediction for regular reinforced concrete buildings using the decision tree algorithm. *Computers and Structures*, *130*, 46–56. https://doi.org/10.1016/j.compstruc.2013.10.006

Ke, G., Meng, Q., Finley, T., Wang, T., Chen, W., Ma, W., Ye, Q., & Liu, T. Y. (2017). LightGBM: A highly efficient gradient boosting decision tree. *Advances in Neural Information Processing Systems*, 2017, Long Beach, CA (pp. 3149–3157).

Kim, J. K., Moon, Y. H., & Eo, S. H. (1998). Compressive strength development of concrete with different curing time and temperature. *Cement and Concrete Research*, *28*(12), 1761–1773. https://doi.org/10.1016/S0008-8846(98)00164-1

Klausen, A. E., Kanstad, T., & Bjøntegaard, Ø. (2019). Hardening concrete exposed to realistic curing temperature regimes and restraint conditions: Advanced testing and design methodology. *Advances in Materials Science and Engineering*, *2019*, 1–15. https://doi.org/10.1155/2019/9071034

Klemczak, B., Batog, M., Giergiczny, Z., & Żmij, A. (2018). Complex effect of concrete composition on the thermo-mechanical behaviour of mass concrete. *Materials*, *11*(11), 2207. https://doi.org/10.3390/ma11112207

Lackner, R., & Mang, H. A. (2004). Chemoplastic material model for the simulation of early-age cracking: From the constitutive law to numerical analyses of massive concrete structures. *Cement and Concrete Composites*, *26*(5), 551–562. https://doi.org/10.1016/S0958-9465(03)00071-4

Lai, S., & Serra, M. (1997). Concrete strength prediction by means of neural network. *Construction and Building Materials*, *11*(2), 93–98. https://doi.org/10.1016/S0950-0618(97)00007-X

Lee, Y., Choi, M.-S., Yi, S.-T., & Kim, J.-K. (2009). Experimental study on the convective heat transfer coefficient of early-age concrete. *Cement and Concrete Composites*, *31*(1), 60–71. https://doi.org/10.1016/j.cemconcomp.2008.09.009

Liang, M., Chang, Z., Wan, Z., Gan, Y., Schlangen, E., & Šavija, B. (2022). Interpretable Ensemble-Machine-Learning models for predicting creep behavior of concrete. *Cement and Concrete Composites*, *125*, 104295. https://doi.org/10.1016/J.CEMCONCOMP.2021.104295

Liang, M., Gan, Y., Chang, Z., Wan, Z., Schlangen, E., & Šavija, B. (2022). Microstructure-informed deep convolutional neural network for predicting short-term creep modulus of cement paste. *Cement and Concrete Research*, *152*, 106681. https://doi.org/10.1016/J.CEMCONRES.2021.106681

Liang, M., Li, Z., He, S., Chang, Z., Gan, Y., Schlangen, E., & Šavija, B. (2022). Stress evolution in restrained GGBFS concrete due to autogenous deformation: Bayesian optimization of aging creep. *Construction and Building Materials*, *324*, 126690. https://doi.org/10.1016/J.CONBUILDMAT.2022.126690

Loh, W.-L. (1996). On Latin hypercube sampling. *The Annals of Statistics*, *24*(5), 2058–2080. https://doi.org/10.1214/aos/1069362310

Lokhorst, S. J. (2001). *Deformational behaviour of concrete influenced by hydration related changes of the microstructure*. Report 25.5-99-05, Delft University of Technology.

Lura, P., van Breugel, K., & Maruyama, I. (2001). Effect of curing temperature and type of cement on early-age shrinkage of high-performance concrete. *Cement and Concrete Research*, *31*(12), 1867–1872. https://doi.org/10.1016/S0008-8846(01)00601-9

Marani, A., Jamali, A., & Nehdi, M. L. (2020). Predicting ultra-high-performance concrete compressive strength using tabular generative adversarial networks. *Materials*, *13*(21), 4757. https://doi.org/10.3390/ma13214757

Maruyama, I., & Lura, P. (2019). Properties of early-age concrete relevant to cracking in massive concrete. *Cement and Concrete Research*, *123*, 105770. https://doi.org/10.1016/J.CEMCONRES.2019.05.015

Myles, A. J., Feudale, R. N., Liu, Y., Woody, N. A., & Brown, S. D. (2004). An introduction to decision tree modeling. *Journal of Chemometrics*, *18*(6), 275–285. https://doi.org/10.1002/cem.873

Olalusi, O. B., & Spyridis, P. (2020). Machine learning-based models for the concrete breakout capacity prediction of single anchors in shear. *Advances in Engineering Software*, *147*, 102832. https://doi.org/10.1016/J.ADVENGSOFT.2020.102832

Pantazopoulou, S. J., & Mills, R. H. (1995). Microstructural Aspects of the Mechanical Response of Plain Concrete. *ACI Materials Journal*, *92*(6), 605–616. https://doi.org/10.14359/9780

Rajashekhar, M. R., & Ellingwood, B. R. (1993). A new look at the response surface approach for reliability analysis. *Structural Safety*, *12*(3), 205–220. https://doi.org/10.1016/0167-4730(93)90003-J

Rasmussen, C. E., & Williams, C. K. I. (2006). *Gaussian processes for machine learning*. MIT Press.

Sagi, O., & Rokach, L. (2018). Ensemble learning: A survey. *WIREs Data Mining and Knowledge Discovery*, *8*(4), e1249. https://doi.org/10.1002/widm.1249

Semianiuk, V., Tur, V., Herrador, M. F., & Paredes, G. M. (2017). Early age strains and self-stresses of expansive concrete members under uniaxial restraint conditions. *Construction and Building Materials*, *131*, 39–49. https://doi.org/10.1016/J.CONBUILDMAT.2016.11.008

Shen, D., Jiang, J., Shen, J., Yao, P., & Jiang, G. (2016). Influence of curing temperature on autogenous shrinkage and cracking resistance of high-performance concrete at an early age. *Construction and Building Materials*, *103*, 67–76. https://doi.org/10.1016/J.CONBUILDMAT.2015.11.039

Shen, D., Liu, K., Wen, C., Shen, Y., & Jiang, G. (2019). Early-age cracking resistance of ground granulated blast furnace slag concrete. *Construction and Building Materials*, *222*, 278–287. https://doi.org/10.1016/J.CONBUILDMAT.2019.06.028

Šmilauer, V., Havlásek, P., Gasch, T., Delaplace, A., Bouhjiti, D. E. M., Benboudjema, F., Briffaut, M., Kanavaris, F., & Azenha, M. (2019). Hygro-mechanical modeling of restrained ring test: COST TU1404 benchmark. *Construction and Building Materials*, *229*, 116543. https://doi.org/10.1016/J.CONBUILDMAT.2019.07.269

Solhmirzaei, R., Salehi, H., Kodur, V., & Naser, M. Z. (2020). Machine learning framework for predicting failure mode and shear capacity of ultra high performance concrete beams. *Engineering Structures*, *224*, 111221. https://doi.org/10.1016/J.ENGSTRUCT.2020.111221

Spingenschmid, R. (1998). *Prevention of thermal cracking in concrete at early ages*. E & FN Spon.

Stute, B., Krupp, V., & von Lieres, E. (2013). Performance of iterative equation solvers for mass transfer problems in three-dimensional sphere packings in COMSOL. *Simulation Modelling Practice and Theory*, *33*, 115–131. https://doi.org/10.1016/j.simpat.2012.10.004

Su, M., Zhong, Q., Peng, H., & Li, S. (2021). Selected machine learning approaches for predicting the interfacial bond strength between FRPs and concrete. *Construction and Building Materials*, *270*, 121456. https://doi.org/10.1016/J.CONBUILDMAT.2020.121456

Taylor, H. F. W. (1997). *Cement chemistry*. Thomas Telford Publishing. https://doi.org/10.1680/cc.25929

Thomas, J. J., Biernacki, J. J., Bullard, J. W., Bishnoi, S., Dolado, J. S., Scherer, G. W., & Luttge, A. (2011). Modeling and simulation of cement hydration kinetics and microstructure development. *Cement and Concrete Research*, *41*(12), 1257–1278. https://doi.org/10.1016/j.cemconres.2010.10.004

Tomar, A., & Burton, H. V. (2021). Active learning method for risk assessment of distributed infrastructure systems. *Computer-Aided Civil and Infrastructure Engineering*, *36*(4), 438–452. https://doi.org/10.1111/mice.12665

Ulm, F.-J., & Coussy, O. (1995). Modeling of Thermochemomechanical couplings of concrete at early ages. *Journal of Engineering Mechanics*, *121*(7), 785–794. https://doi.org/10.1061/(ASCE)0733-9399(1995)121:7(785)

Turcry, P., Loukili, A., Barcelo, L., & Casabonne, J. M. (2002). Can the maturity concept be used to separate the autogenous shrinkage and thermal deformation of a cement paste at early age? *Cement and Concrete Research*, *32*(9), 1443–1450. https://doi.org/10.1016/S0008-8846(02)00800-1

Wan, Z., Xu, Y., & Šavija, B. (2021). On the use of machine learning models for prediction of compressive strength of concrete: influence of dimensionality reduction on the model performance. *Materials*, *14*(4), 713. https://doi.org/10.3390/ma14040713

Xin, J., Zhang, G., Liu, Y., Wang, Z., & Wu, Z. (2020). Evaluation of behavior and cracking potential of early-age cementitious systems using uniaxial restraint tests: A review. *Construction and Building Materials*, *231*, 117146. https://doi.org/10.1016/J.CONBUILDMAT.2019.117146

Ye, G., Breugel, K. V., & Fraaij, A. L. A. (2003). Experimental study and numerical simulation of the development of the microstructure and permeability of cementitious materials. *11th International Congress on the Chemistry of Cement*, Durban, South Africa.

Yang, J., Wang, Q., & Zhou, Y. (2017). Influence of curing time on the drying shrinkage of concretes with different binders and water-to-binder ratios. *Advances in Materials Science and Engineering*, *2017*, 1–10. https://doi.org/10.1155/2017/2695435

Yuan, Y., Au, F. T. K., Yang, D., & Zhang, J. (2022). Active learning structural model updating of a multisensory system based on Kriging method and Bayesian inference. *Computer-Aided Civil and Infrastructure Engineering.*, Advance online publication. https://doi.org/10.1111/mice.12822

Zhang, J., Ma, G., Huang, Y., sun, J., Aslani, F., & Nener, B. (2019). Modelling uniaxial compressive strength of lightweight self-compacting concrete using random forest regression. *Construction and Building Materials*, *210*, 713–719. https://doi.org/10.1016/j.conbuildmat.2019.03.189

Zhao, H., Jiang, K., Hong, B., Yang, R., Xu, W., Tian, Q., & Liu, J. (2021). Experimental and numerical analysis on coupled hygro-thermo-chemo-mechanical effect in early-age concrete. *Journal of Materials in Civil Engineering*, *33*(5), 04021064. https://doi.org/10.1061/(ASCE)MT.1943-5533.0003666

Zhao, H., Jiang, K., Yang, R., Tang, Y., & Liu, J. (2020). Experimental and theoretical analysis on coupled effect of hydration, temperature and humidity in early-age cement-based materials. *International Journal of Heat and Mass Transfer*, *146*, 118784. https://doi.org/10.1016/j.ijheatmasstransfer.2019.118784

How to cite this article: Liang, M., Chang, Z., He, S., Chen, Y., Gan, Y., Schlangen, E., & Šavija, B. (2022). Predicting early-age stress evolution in restrained concrete by thermo-chemo-mechanical model and active ensemble learning. *Computer-Aided Civil and Infrastructure Engineering*, 1–25. https://doi.org/10.1111/mice.12915